International Journal of Thermal Sciences 211 (2025) 109716

Contents lists available at ScienceDirect

International Journal of Thermal Sciences

journal homepage: www.elsevier.com/locate/ijts

Performance comparison and mechanism analysis of new gas-liquid dimpled plate heat exchangers(DPHE) involving condensation

Xiang Liu, Fengyongkang Wu, Xue Xue, Kelang Jin, Lei Zhang, Hao Zhou *

Zhejiang University, Institute for Thermal Power Engineering, State Key Laboratory of Clean Energy Utilization, Hangzhou, 310027, PR China

ARTICLE INFO

Keywords:
Gas-liquid DPHE
Structural optimization
Exothermic condensation
Computational fluid dynamics
Mechanistic analysis

ABSTRACT

Gas-liquid dimpled plate heat exchanger (DPHE) is an effective tool for recovering waste heat from the exhaust gases of heat recovery boilers. This study tested the pilot performance of three new DPHEs and used computational fluid dynamics (CFD) to analyze the internal flow and heat transfer mechanisms. 3rd DPHE achieved superior convective heat transfer coefficients, reaching 135 W/(m^2·K) at flue gas flow rate of 10,000 m^3/h, with latent heat accounting for 40 % of the total heat transfer. In contrast, the 2nd DPHE performed less efficiently due to insufficient latent heat transfer, contributing only 25 %. Larger dimple spacing stabilized the flue gas flow, reducing unstable vortices and the effective heat transfer area. As the flow rate increased, latent heat, sensible heat, and pressure drop all increased linearly. *Re-Nu* and *Re-f* models fill the data gap for heat exchange with low-temperature flue gases in the transitional flow regime. Simulation results show that the initial dimple at the inlet is the main source of pressure loss, accounting for approximately 20 % of the total pressure drop. Adjusting the dimple angle can rapidly reduce the pressure loss. The macroscopic heat transfer mechanism of 3rd DPHE involves twisted dimples that promote uniform flow distribution on the waterside and enhance flue gas turbulence, thereby improving the heat exchange process. Additionally, the cold-side flow field distribution uniformly expands the condensation area (45 % vs. 25 %), rather than altering the heat transfer mode. Reducing dimple spacing and increasing the twist angle are the optimal solutions for enhancing heat transfer efficiency and reducing pressure loss.

Nomenclature

Q_f	Flue gas exothermic power [kW]	*Re*	Reynolds number
t'	Inlet temperature [K]	*Nu*	Nussle number
t'	Outlet temperature [K]	*f*	Fanning friction factor
C_p	Specific heat capacity [J/(kg·K)]	*D*	Characteristic length of inlet [m]
Q_l	Condensation power [kW]	*h*	Heat transfer coefficient [W/(m^2·K)]
M	Molar mass of water	ΔP	Pressure loss of the DPHE in flue gas [Pa]
R	Ideal gas constant J/(mol·K)	*L*	Flow distance in the DPHE [m]
P	Pressure [Pa]	ρ	Average density [kg/m^3]
Y	Volume fraction of water vapor	**u**	Flow rate of the medium [m/s]
V	Volumetric flow rate [m^3/s]	μ	Average dynamic viscosity of the flue gas [Pa·s]
m	Mass flow rate [kg/s]	*t*	The thickness of the plate [m]
Q_t	Average heat transfer power [kW]	λ	Thermal conductivity [W/(m·K)]

(*continued on next column*)

(*continued*)

U	Overall heat transfer coefficient [W/(m^2·K)]	Δt_m	Mean logarithmic temperature difference [K]
A	Total effective heat transfer area [m^2]	*T*	Temperatures of the different phases in the computational cell [°C]
g	gravitational acceleration [m/s^2]	τ	Shear stress between different phases in the computational cell [kg·m/s^2]
S	The source of additional mass for the interphase transformation [kg/m^3·s]	**F**	The interfacial force between the different phases [kg/m^2·s^2]
	Subscript		
f	subscript indicates the flue gas	*s*	subscript indicates the steel
vap	subscript indicates water vapor	*w*	subscript indicates water
con	subscript indicates condensation		

1. Introduction

Climate warming and the shortage of energy have become problems

* Corresponding author.
E-mail address: zhouhao@zju.edu.cn (H. Zhou).

https://doi.org/10.1016/j.ijthermalsci.2025.109716
Received 30 April 2024; Received in revised form 22 December 2024; Accepted 15 January 2025
Available online 28 January 2025

that must be seriously considered for the development of society, which is the largest public crisis encountered by humanity [1]. Energy conservation, emission reduction, improving energy efficiency, and reducing greenhouse gas emissions are the inevitable trends for future national energy development [2]. Research on efficient and reliable heat exchanger equipment effectively solves the above problems, and developing compact heat exchangers is the optimization direction [3]. Plate heat exchanger (PHE) is a compact device composed of corrugated plates arranged at specific inclination angles, creating fluid flow and heat transfer pathways between the plates [4,5]. High and low-temperature fluids traverse distinct flow paths, low-temperature fluid is surrounded by high-temperature fluid on both sides with double-side heating. Conversely, high-temperature fluid is surrounded by low-temperature fluid with double-side cooling. Compared to traditional shell and tube heat exchangers, PHE can achieve a 3 to 5 times increase in heat transfer coefficient, which reduces footprints and lowers operating costs for the same heat transfer capacity. However, due to the more complex internal flow structure compared to other heat exchangers, researchers worldwide are actively engaged in making improvements and continuously proposing new flow design structures [6].

PHEs can be categorized into three types, Plate-and-Frame PHEs, Brazed PHEs (BPHE) and Welded PHEs. Regardless of their types and forms, the core of the PHE is the corrugated plate pack [7]. Structural parameters of the corrugate and twist angle of the internal structure have significant impacts on the performance of PHEs. It is essential to draw on the relevant basis from the existing literature and carry out simulation or experimental verification to design novel PHE with excellent performance. Currently, Chevron plate heat exchangers (CPHEs) enjoy the highest market penetration, and extensive research has been conducted on their flow and heat transfer processes. The geometric analysis of CPHE mainly focuses on the V-shaped angle. Li et al. [8] used numerical methods to investigate the effects of chevron angles ($\beta = 30^\circ, 45^\circ, 60^\circ$), corrugation heights (H = 3, 5, 7, 9 mm), and pitch (P = 15, 20, 30, 45, 60 mm) on flow and heat transfer, and obtained the optimal solution. Focke et al. [9] explored the trends of *Nu* (Nussel number) and *f* (friction factor) based on the changes in corrugation angles, and found that different flow regimes occur on both sides of 60°. Zimmerer et al. [10] used visualization to obtain mechanisms for flow regime variation with the V-angle. The effect of V-angle and expansion coefficient of the corrugated area on heat transfer and flow resistance was also experimentally investigated by Muley et al. [11]. Contemporary scholars are deeply concerned with various factors such as the form, angle, spacing, and area of corrugations, thereby providing valuable design insights for new PHEs. The heat transfer properties of special fluids such as nanofluids and supercritical CO_2 within PHEs have also been scrutinized. Zheng et al. [12] experimentally investigated the performance of nanofluids in a PHE, where Fe_3O_4-water and CuO-water nanofluids showed the best and worst heat transfer performance. Zendehboudi et al. [13] investigated the heat transfer and pressure drop performance of supercritical CO_2 in brazed PHEs and clarified the thermal resistance on the CO_2 side is the main factor affecting the total heat transfer. Zhang et al. [14] proposed a novel waste heat recovery device for high-temperature exhaust gases, featuring multiple insert combinations in gradient recovery heat exchangers. This design achieves a 25 % improvement in efficiency and a lower pressure drop compared to traditional spiral insert heat exchangers. Zhang et al. [15] investigated heat transfer in a flue gas heat recovery unit using a real-time measurement database and derived a dimensionless relational equation to account for condensation energy. Although experimental methods can accurately capture the thermo-hydraulics of PHEs, the studies are constrained by platform construction and associated costs. In addition, it is difficult for researchers to observe the fluid flow in the entire field to get the mechanism behind the variation of heat exchanger performance. With the progress of numerical simulation, computational fluid dynamics (CFD) has become an instrumental tool that complements experimental methods. In recent years, many scholars have utilized CFD to research and develop new types of PHEs.

Single-phase laminar flow of highly viscous fluid inside a PHE was simulated by Han et al. [16] and obtained pressure, temperature, and velocity field distributions. Based on numerical calculations, Mahmood et al. [17] discovered that secondary flows were generated at the concave-convex unit. Khail et al. [18] investigated the heat transfer and mass transfer performance of dimple formation with a hyperbolic tangent function shape under single-phase flow conditions, and found that longitudinal turbulence has a greater impact on heat transfer than transverse turbulence. Duan et al. [19] developed a PHE suitable for thermal recovery of oilfield wastewater. Simulation results showed that the corrugation height significantly influences the average *Nu* and pressure drop in the corrugated channels. Tran et al. [20] determined the heat transfer capabilities of corrugated PHE within Re ranging from 700 to 8000. Under optimal combinations of wave amplitude, plate spacing, plate thickness, plate length, and plate height, the maximum heat transfer coefficient achieved was 150 $W/(m^2 \cdot K)$.

Tang et al. [21] studied the performance of a novel H-type finned tube heat exchanger within the Re range of 6833–20500. The results indicated that the optimal fin size combination at Re = 7000 corresponds to *Nu* of approximately 40. Nguye et al. [22] proposed an innovative PHE design with symmetric wing-shaped corrugations and studied the effects of corrugation angle, spacing, reflector arrangement, and small wing profiles on heat transfer performance. The results showed that the corresponding *Nu* ranged from 60 to 100 for Re between 4600 and 8400. Han et al. [23] developed a novel heat exchanger utilizing wing fins and established the dimensionless equation, showing that when the flue gas side Re from 1300–1600, the corresponding *Nu* is 13. Feng et al. [24] proposed a novel H-type integrally formed spiral finned tube heat exchanger for waste heat recovery. Additionally, the relationship between Re and *Nu* was established through simulations, with *Nu* ranging from 30 to 100 corresponding to Re between 5000 and 45000. All the results indicated that CFD is an excellent tool for studying heat transfer and mass transfer mechanisms.

In recent years, researchers have continuously proposed other forms of PHEs. Jiang et al. [25] designed capsule-PHE and used numerical simulations to elucidate the influence of capsule geometry on heat transfer performance. Their findings demonstrated that capsule-PHEs show higher heat transfer coefficients and lower frictional pressure drops in comparison with CPHEs. Fluid impingement and vortex generation play a crucial role in optimizing heat transfer performance. Xuan et al. [26] introduced the Dimpled plate heat exchangers(DPHE), which incorporate secondary flow and disrupt the boundary layer [27,28]. Dimples can be asymmetric and generate vortices to alleviate fouling. DPHE combines the advantages of flexible flow section area and counterflow, making it a research focus for novel low-temperature PHEs. The dual carbon strategy has promoted the widespread application of gas turbines. Consequently, how to efficiently recover waste heat from combustion turbine exhaust has become a priority for heat supply in northern China. Gas turbine exhaust often contains a large amount of water vapor, and the condensation of the vapor in the heat exchanger is a complex process [29]. Therefore, research and development of gas-liquid PHEs containing condensing vapors is a trend in heat exchanger research. Intensity of vapor condensation in PHEs depends on different factors, including the geometry of the flow path, the heat exchanger surface material and the thermophysical properties of the condensed material [30,31]. Eldeeb et al. [32] discussed the utilization of empirical equations to obtain heat transfer coefficients for vapor condensation, but mainly for refrigerants. For vapor condensation, the semi-empirical formulas proposed by Tovazhnyanski et al. [33] and Thonon et al. [34] have excellent accuracy in predicting the heat transfer coefficients but only take into account pure steam condensation processes. Ambrosini et al. [35,36] studied the heat transfer characteristics of steam and natural gas mixtures in heat exchangers using stagnation film and turbulent boundary layer theories. They suggested that the correlation method can be used to calculate the convective heat

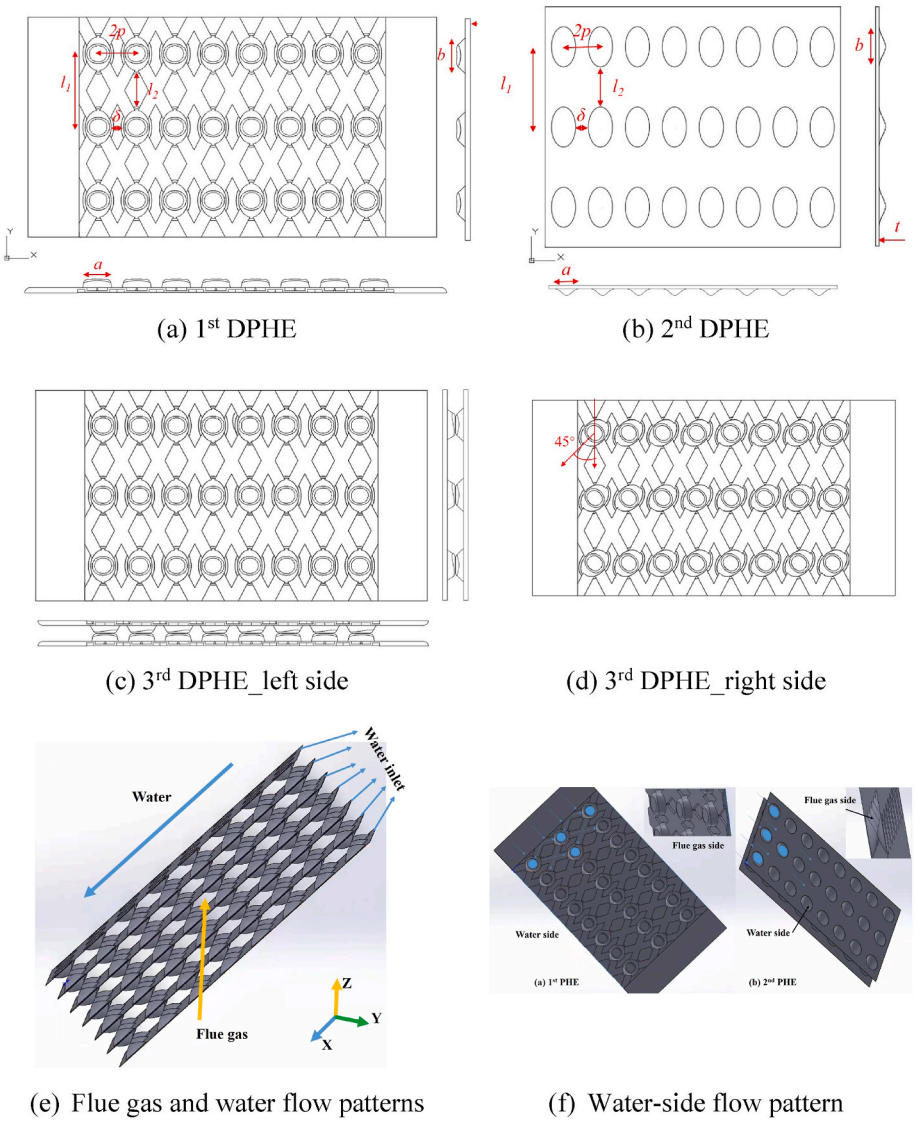

Fig. 1. Three types of DPHE sizes and specifications.

Table 1
Detailed dimensions of the three DPHEs.

	l_1 (mm)	l_2 (mm)	δ (mm)	t (mm)	$2p$ (mm)	a (mm)	b (mm)	θ
1st DPHE	25	10	1	1.5	11	10.5	15	0
	50	25	1	1	8	15	25	0
2nd DPHE								
	25	10	1	1.5	11	10.5	15	45°
3rd DPHE								

transfer coefficient for single-phase flow. In addition, the pressure drop of the two-phase flow of mixed steam and condensed liquid in the microchannel is also significant. Kim et al. [37] employed experimental methods to obtain pressure drop data for two-phase flow in microchannels, but no analogies can be drawn within other channels. Kapustenko et al. [38] developed one-dimensional mathematical model for portraying the pressure drop of air-steam in PHE with a relative average error of only 11.4 %. In conclusion, the new PHE to recover waste heat from flue gas-containing steam is a challenging and meaningful research point.

A thermal power plant in northern China uses natural gas to realize dual electricity and heat output. However, the high-temperature flue gas emissions during operation hinder the maximization and deep utilization of natural gas energy. Exhaust flue gas from the gas turbine often contains a certain amount of water vapor. Heat transfer process will generate certain amount of condensation by forming gas-liquid two-phase flow, which constitutes the difficulty and focus of the current development of the new PHE. In this study, three new DPHEs involving condensation for industrial applications are proposed and the optimal dimpling form is clarified based on the performance test with 10000 m^3/h flue gas on the pilot platform. The optimal dimple form and mechanism are determined based on heat exchange and pressure loss tests in the pilot platform, which have been proven to outperform other flue gas waste heat recovery devices in the literature. Dimensionless relationship equations of three DPHEs are derived and analyzed to provide the theoretical basis for the subsequent modification. Additionally, the

Table 2
Measurement uncertainty of each parameter in the system.

Measured parameter	Flow rate/ (m^3/h)	Temperature/K		Pressure/ MPa	Differential pressure/kPa
Accuracy (tolerance value)	1 %	±0.15	±0.15	1.6 %	2.5 %
Range	0–50	273–1273	273–1273	0–0.4	0–200
Location	Cold	Cold	Hot	Cold	Hot

mechanism of heat exchanger performance enhancement was studied based on CFD, and the main reasons affecting heat exchanger performance were clarified, which provides the direction and ideas for developing a new type and high-efficiency heat exchanger.

2. Experimental system and process

2.1. Basic parameters of three types of DPHEs

Three views and corresponding parameters of the three DPHEs are presented in Fig. 1 and Table 1. In this study, the proposed DPHEs are fabricated from single plates formed by mold stamping. Two plates are brazed together to form the water-side flow channels. Finally, two sets of plates are stacked to create the test module. Flow behavior of flue gas and water is illustrated using the 2nd DPHE as an example. As shown in Fig. 1 (e), the flue gas flows along the +Z direction, and sweeps across the dimples for heat exchange, while the water flows downward along the +X direction, with the flow directions of the gas and water being at 90°. 1st DPHE has cross-flow channels between the dimples to facilitate the migration and aggregation of water. 3rd DPHE is of the same type as the 1st DPHE. However, the dimple on one side of the plate is rotated 45° towards the -X direction in the 3rd DPHE. Cooling water flows through the cross-flow channels and dimples, while high-temperature flue gas sweeps across the dimples in the gap. 2nd DPHE also has dimples but lacks the cross-flow channels connecting the dimples. Water flows through the gaps between the two plates and aggregates in the dimples as shown in Fig. 1 (f).

In comparison with the 1st and 3rd DPHEs, the 2nd DPHE has smaller dimple pitch and flatter, larger dimple. The longitudinal spacing of the dimples in the 1st DPHE is half that of the 2nd DPHE, and the dimple height in the 1st DPHE is also greater than that in the 2nd DPHE. The different dimple shapes lead to significantly different flue gas flow patterns. The comparison of these two basic DPHEs provides insights into how dimple height and spacing specifically affect heat transfer performance.

2.2. Measurement uncertainty of test media and parameters

The media on both sides of the heat transfer surface is flue gas and water, with flue gas on the hot side and water on the cold side. Parameter measurement uncertainty was shown in Table 2. All temperature data were collected in real-time by Agilent (Agilent 34970A), and the data were collected once every 6 s and transferred to the computer for recording. An electromagnetic flow meter collected the flow rate in real time, and RS485 was used to communicate with the computer. The inlet and outlet pressure on cold side were displayed by shockproof pressure gauges and collected by manual readings. In a specific set of experimental conditions, the water-side pressure was determined by averaging three readings. Measuring holes were punctured at the center of both the front and back sides of the flue gas. The four measuring holes in this section were interconnected in parallel through copper tubing to measure the flue gas pressure. The pressure drop before and after the experimental section was measured using a rubber hose connected to the Testo 435 multifunction meter. The vapor fraction content of the flue gas was measured by using an HMS545P portable water meter in flue gas with an instrumental measurement uncertainty of ±2 %. Flue gas flow rate was obtained using the Testo 435 multifunction meter.

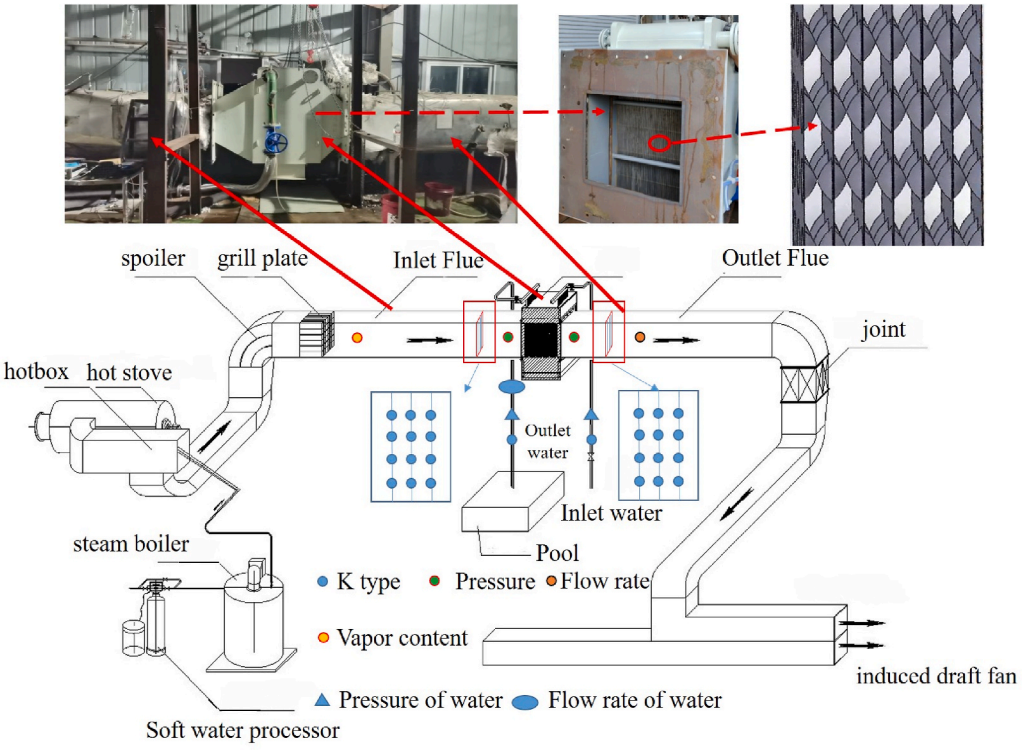

Fig. 2. Flow diagram of the experimental system.

Table 3
Parameter statistics for test cases.

Variable	unit	Case 1	Case 2	Case 3	Case 4
Inlet flow rate of flue gas	m^3/h	9600	8100	13000	6800
Inlet temperature of flue gas	K	348.00	348.00	348.00	348.00
Water content in flue gas	g/kg	48	48	48	48
Inlet flow rate of cold water	m^3/h	22.00	22.00	22.00	22.00

2.3. Experimental system and procedure

The schematic diagram of the experimental system is shown in Fig. 2 and the whole experiment is carried out in a hot air duct, including a flue gas system, parameter measurement system and tap water system. Fig. 2 gives a field photo of the horizontal flue and the test module with the specific form of dimples inside the heat exchanger. The relevant instruments and corresponding operational procedures were also clarified. OIL BURNER(BT 75LR, min: 35 kg/h, 415 kW; max: 75 kg/h, 889 kW) produces hot flue gas by burning oil, and inducer fan(1450 rpm and 45 kW) brings the flue gas into the DPHEs for heat exchange with the cold medium. Finally, the exchanged flue gas is discharged into the environment through the chimney. All pipelines were covered with a certain thickness of insulation cotton to reduce heat loss. Measurement system includes Agilent 34970A, Testo 435 multifunction meter, and HMS545P portable water meter. Remaining instruments are flow meters and thermometers. All parameters that should be measured during the experiment are the inlet and outlet flue gas (cold water) temperature, flue gas (cold water) flow rate, pressure drop, and water vapor content before and after the experimental section. The average temperature is taken as the inlet and outlet flue gas temperatures which are measured by 12 thermometers as shown in Fig. 2, reducing the measurement error. Specific experimental steps are as follows.

(1) Activate the soft water processor and steam boiler to generate steam;
(2) Start the induced draft fan and oil burner to produce flue gas;
(3) Adjust the inlet flue gas flow and the oil supply pressure of the oil burner to regulate the inlet flue gas temperature, until it approaches the target value for the test condition;
(4) Open the steam valve and continuously adjust it to approach the target value;
(5) Re-adjust the oil supply pressure to maintain the inlet flue gas flow, temperature, and steam concentration at the target values, then begin the experiment;
(6) Record the Agilent time when the three variables align with the target values to obtain 26 temperature points and the water flow rate. Simultaneously, the flue gas flow, pressure drop and the inlet water vapor concentration were measured (averaged over 40 s to measure fluctuations);
(7) Repeat each experimental condition six times to minimize errors in subsequent data processing.

In this study, three DPHEs were evaluated on the pilot platform and the specific experimental conditions are outlined in Table 3 below. Cases 1, 2, and 3 were conducted for 2nd and 3rd DPHEs, while 1st DPHE was tested for cases 1, 2, and 4. The only variation was the flue gas flow rate, while vapor content and flue gas temperature were maintained constant. The flow and heat transfer performance of different DPHEs are evaluated by varying the flue gas velocity, enabling a comparison of the DPHEs.

3. Data processing process

3.1. Basic data processing

Heat-transferred power was used to describe the heat exchanger performance, flue gas exothermic power Q_f is calculated using Eq. (1), m_f is flue gas mass flow rate, kg/s; t_f' is inlet flue gas temperature, K; t_f'' is outlet flue temperature, K; $c_{p,f}$ is the specific heat of flue gas at constant pressure, J/(kg·K). Q_l is water vapor condensation power of flue gas, calculated by determining the volume fraction of water vapor before and after the heat exchange process as shown in Eq. (2). M and R are the molar mass of water and the ideal gas constant, respectively. P_{vap} is the partial pressure of water vapor, Y is the measured volume fraction of water vapor and V is the volumetric flow rate of the flue gas, m^3/s.

$$Q_f = Q_s + Q_l = m_f\left(t_f' - t_f''\right)c_{p,f} + Q_l \tag{1}$$

$$Q_l = \dot{m}_{con}\,\Delta H = \Delta H\left(\frac{2MP'_{vap}Y'_{vap}V}{R\left(t_f' + t_f''\right)} - \frac{2MP'_{vap}Y'_{vap}V}{R\left(t_f' + t_f''\right)}\right) \tag{2}$$

$$Q_w = m_w(t_w'' - t_w')c_{p,w} \tag{3}$$

Eq. (3) was used to calculate the power absorption of water, m_w is the mass flow rate of water, kg/s; t_w' is inlet water temperature, K; t_w'' is outlet water temperature, K; $c_{p,w}$ is specific heat of water at constant pressure, J/(kg·K). The average heat transfer power Q_t was calculated using Eq. (4); U is the total heat transfer coefficient, W/(m^2·K); A is total effective heat transfer area, m^2; Δt_m is the mean logarithmic temperature difference of countercurrent arrangement, K; U of the DPHE can be obtained by combining Eqs. (4)–(7).

$$Q_t = \left(Q_f + Q_w\right)/2 \tag{4}$$

$$Q_t = UA\Delta t_m \tag{5}$$

$$U = \frac{\left(Q_f + Q_w\right)/2}{A\cdot\Delta t_m} \tag{6}$$

$$\Delta t_m = \frac{\left(t_f' - t_w''\right) - \left(t_f'' - t_w'\right)}{\ln\frac{t_f' - t_w''}{t_f'' - t_w'}} \tag{7}$$

3.2. Deep data processing

Re, *Nu* and *f* are essential indicators for evaluating the performance of novel DPHEs, and the calculation equations are as shown in Eq. (8), where D indicates the characteristic length of the inlet is obtained by the basic calculation of 4 times the flow area divided by the perimeter of the flow area, m; λ indicates the thermal conductivity, W/(m·K); h indicates the heat transfer coefficient, W/(m^2·K); ΔP indicates the pressure loss of the flue gas passing through the DPHE, Pa; L indicates the flow distance in the DPHE, m; ρ indicates the average density in the DPHE, kg/m^3; u indicates the flow rate, m/s; μ indicates the average kinetic viscosity flowing through the DPHE, Pa·s.

$$Nu = \frac{Dh}{\lambda} \quad f = \frac{2D\Delta P}{L\rho u^2} \quad \mathrm{Re} = \frac{\rho Du}{\mu} \tag{8}$$

h_f in the above equation is calculated by Eq. (9), wherein t denotes the thickness of the DPHE, m; λ_s denotes the thermal conductivity of the DPHE, W/(m·K); h_w is the convective heat transfer coefficient of the waterside, W/(m^2·K); wherein h_w is an unknown quantity, and the *Nu* of waterside is obtained by Eq. (10) [39]. In summary, the heat transfer coefficient h_f on the flue gas side can be obtained through U, h_w, and t, which leads to a series of dimensionless numbers.

Table 4
Uncertainty of indirect parameters.

Experimental parameters	Maximum uncertainty (%)
Q_s	2.20 %
Q_l	2.00 %
Q_t	1.74 %
U	1.98 %
Re	1.00 %
Nu	2.42 %

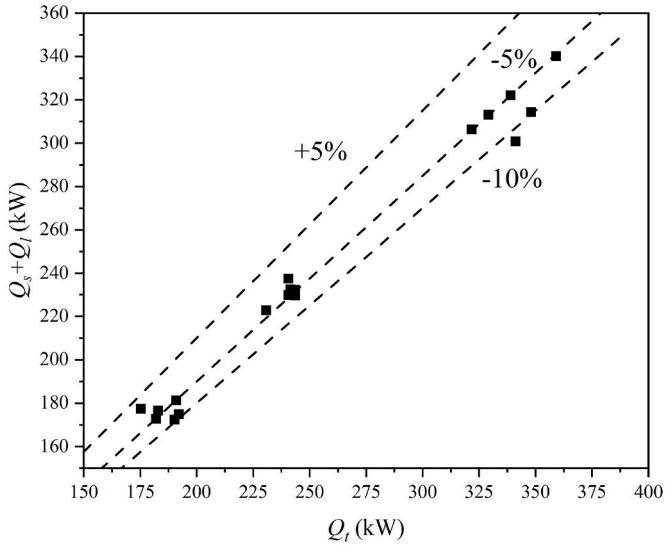

Fig. 3. Energy balance validation of hot side (flue gas) and cold side (water side).

$$U=\frac{1}{\frac{1}{hf}+\frac{t}{\lambda_s}+\frac{1}{h_w}} \tag{9}$$

$$Nu_w=3.66+\frac{0.0668\mathrm{Re}_w\,\mathrm{Pr}_w(D_w/L_w)}{1+0.04[(D_w/L_w)\mathrm{Re}_w\,\mathrm{Pr}_w]^{2/3}} \tag{10}$$

3.3. Uncertainty analysis

Many quantities often cannot be measured directly in scientific experiments and production practice, requiring indirect measurement methods. *Q*,*U,* Re *and Nu* cannot be measured directly and must be obtained by measuring elements, flow rate, temperature and other factors. Indirectly measured quantity N is obtained from the directly measured quantities x y through the functional relation $N = f(x, y, \ldots)$. Since there are errors in the direct measurement devices, there must be uncertainties in the indirect measurement elements as well. Considering the statistical nature of the uncertainty synthesis, the "square and root" synthesis is generally used to estimate the standard uncertainty of indirect measurements. If the indirect measurement N is the sum or difference function of the direct measurements x, y, and z, it is more convenient to use Eq. (11) to calculate ΔN; if the indirect measurement N is the product or quotient function of the direct measurements x, y, z, the relative uncertainty of $\Delta N/N$ was calculated first and then calculated ΔN through the relative uncertainty. This study calculates Q, U, Re and Nu from the directly measured elements, and specific uncertainty formulas are given in Eqs. (13) and (14). Results of uncertainty calculations for each experimental parameter are shown in Table 4. In addition, typical calculation procedures and corresponding program codes for Nu and Re can be found in Supporting Material ***S1***. The uncertainties for both Re and Nu are not greater than 3 % respectively due to the use of mercury and higher precision electronic thermometers.

$$\Delta N=\sqrt{\left(\frac{\partial f}{\partial x}\right)^2\Delta_x^2+\left(\frac{\partial f}{\partial y}\right)^2\Delta_y{}^2+\left(\frac{\partial f}{\partial z}\right)^2\Delta_z{}^2} \tag{11}$$

$$\frac{\Delta N}{N}=\frac{1}{N}\sqrt{\left(\frac{\partial f}{\partial x}\right)^2\Delta_x^2+\left(\frac{\partial f}{\partial y}\right)^2\Delta_y^2+\left(\frac{\partial f}{\partial z}\right)^2\Delta_z{}^2} \tag{12}$$

$$\Delta Q=\sqrt{\left[\frac{\partial Q}{\partial m}\Delta m\right]^2+\left[\frac{\partial Q}{\partial t'}\Delta t'\right]^2+\left[\frac{\partial Q}{\partial t'}\Delta t'\right]^2} \tag{13}$$

$$\Delta U=\sqrt{\left[\frac{\partial U}{\partial Q}\Delta Q\right]^2+\left[\frac{\partial U}{\partial t_1{}'}\Delta t'\right]^2+\left[\frac{\partial U}{\partial t_1{}'}\Delta t'\right]^2+\left[\frac{\partial U}{\partial t_2{}'}\Delta t_2{}'\right]^2+\left[\frac{\partial U}{\partial t_2{}'}\Delta t_2{}'\right]^2} \tag{14}$$

4. Results and discussion

4.1. Comparison of basic working conditions of three DPHEs

Fig. 3 shows that the error between the flue gas side and water side of the heat exchanger is approximately 5 %, which meets ANSI/ASHRAE 33 Standards. The accuracy of the system was ensured, and the experimental data were calibrated subsequently. Case 1 serves as the basic condition for comparing the variation trends of critical parameters for the three DPHEs. As can be seen from Fig. 4 (a), four comparison parameters were selected, which are Q_s, Q_l, Q_t, and U. First, Q_s of the three DPHEs are not significantly different, which of the 3rd DPHE is the largest, followed by 2nd DPHE and 1st DPHE. The Q_l of 1st and 3rd DPHE is significantly higher than that of 2nd DPHE (about 1.5 times of 2nd DPHE), indicating that the latent heat transfer mechanism of 1st DPHE and 3rd DPHE was inconsistent with that of 2nd DPHE. Internal flow channel structure of 1st and 3rd DPHE can significantly promote the condensation and heat release of water vapor in flue gas. When comparing Q_t of the three heat exchangers, the 3rd DPHE has the highest heat transfer power, about 240 kW, followed by the 2nd and 1st DPHE. The difference in heat transfer capacity of different heat exchangers is mainly caused by the significant difference in Q_l, which also indicates the main research direction of developing new DPHE. Larger dimple spacing results in more stable flue gas flow, reducing unstable eddies and the Coanda effect, thereby lowering the overall heat transfer performance. Moreover, longer dimple spacing reduces the water-flue gas heat exchange area, thus weakening the heat transfer performance. However, although turbulence enhances heat transfer, it also increases pressure loss, leading to high-pressure losses in subsequent heat recovery devices, causing the gas turbine to operate abnormally. Moreover, the 3rd DPHE has the highest U under the same condition, about 125 W/(m^2·K). Although the Q_t of 1st DPHE is higher than that of 2nd DPHE, the U of the two is almost the same 100 W/(m^2·K), mainly because the heat transfer area of 2nd DPHE is smaller than that of 1st DPHE. Nevertheless, the experimental results of the three DPHEs are significantly higher than the convective heat transfer coefficient of other DPHEs proposed by Lin et al., about 25~70 W/(m^2·K) [40]. This indicates that the three DPHEs proposed in this work have better performance, especially the 3rd DPHE, which will be discussed in detail below.

Fig. 4 (b) (c) (d) shows the changing trend of heat transfer parameters concerning the flow rate. Although 1st DPHE and 3rd DPHE belong to the same plate type, their characteristics exhibit significant differences. As shown in Fig. 4(b) and (d), the U of the two DPHEs shows different trends as the flow rate changes and the U of the 1st DPHE plate increases rapidly with the flow rate increase. Conversely, the U of the 3rd DPHE tends to stabilize with an increase in flow rate. This phenomenon is primarily attributed to the significant alteration of the flow field caused by torsional dimple, as evidenced by the substantial difference in pressure loss. High flow rates corresponding to larger U values indicate that the maximum flue gas handling capacity of 3rd DPHE

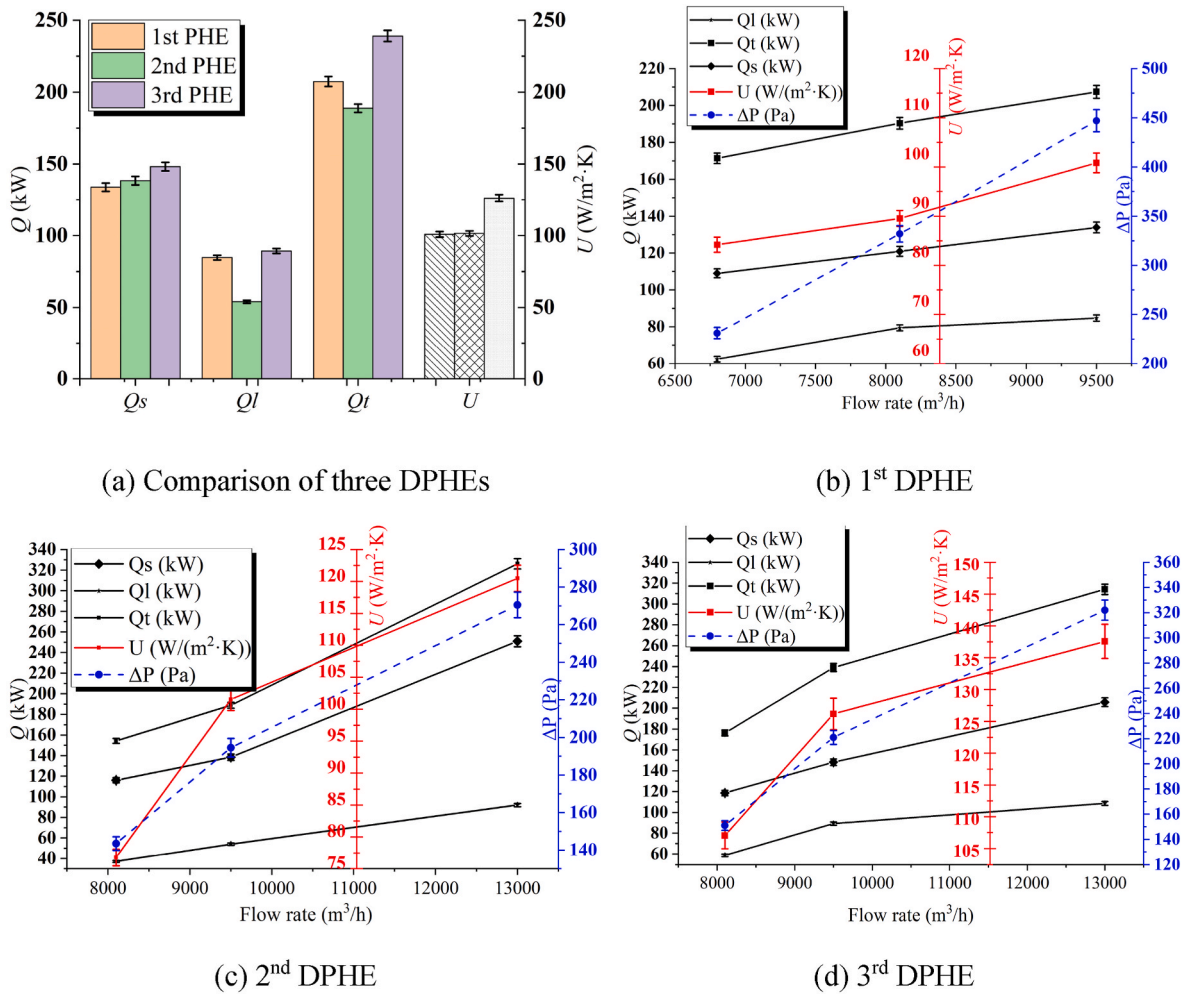

Fig. 4. Comparison of basic working conditions of three DPHEs and the variation trend of each PHE parameter with flue gas flow rate.

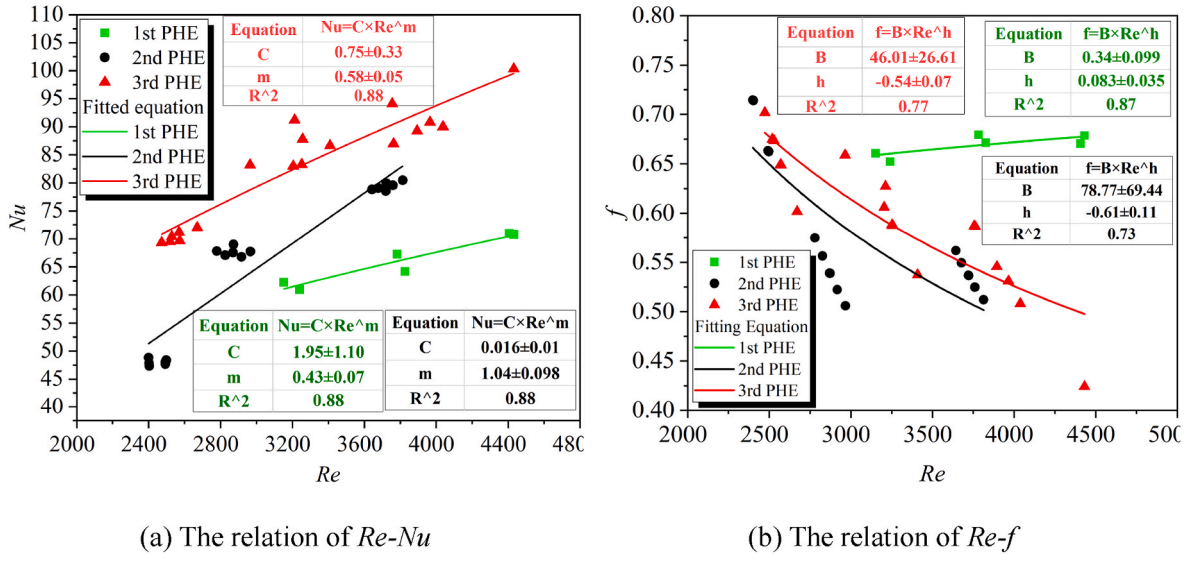

Fig. 5. The *Re-Nu* dimensionless relationship of three DPHEs and the comparison dimensionless relationship of *f-Re*.

exceeds that of 1st DPHE, which is already at a bottleneck near the test conditions. Besides differing trend variations, the U of the two DPHEs also exhibit notable differences. At the same flow rate, U is approximately 90 W/(m^2·K) for 1st DPHE and about 108 W/(m^2·K) for 3rd DPHE, indicating a significant disparity. Of course, the exact reason needs to be further clarified with the help of transparent DPHE or CFD, which were discussed in the following chapter. In addition, Q_s, Q_l, and Q_t all increase continuously with the change in flow rate, as shown in

Table 5
Results of previous studies for comparison.

Heat exchange medium	Heat exchanger configuration	*Nu*-*Re* or *h*-*Re*	Comparison point	References
Hot air-cold water	Airfoil fins heat exchanger	*Nu*:11–15 *Re*:800~2100	Re = 2100 *Nu* = 15	Reference [23]
Oil-gas-water three-phase fluid	PHE	*Nu*:60–150 *Re*:3000~12000	Re = 4500 *Nu* = 80	Reference [19]
Flue gas-water	Condensing flue-gas heat recovery unit	*Nu*:10–33 *Re*:696~2172	Re = 2172 *Nu* = 33 On-site	Reference [15]
Hot air-cold medium	Air-foil corrugated PHE	*Nu*:70–120 *Re*:4500~8500	Re = 4500 *Nu* = 70	Reference [22]

Fig. 4. However, there must be a fixed value of *Q*, which will not change with an increasing flow rate to maximum processing capacity. The trends in critical parameters can reflect the differences in heat exchange modes to a certain extent. The *U* value of 2nd DPHE gradually tends to be gentle with the flow rate change, indicating that the 2nd and 3rd DPHE may have the same flow and heat transfer processes. Turbulence enables 3rd DPHE to have the best heat exchange capabilities, although it may have higher pressure losses. By examining the pressure losses, it is evident that the 3rd and 2nd DPHE have the most minor pressure losses, about 160 Pa, while 1st DPHE has the highest, approximately 350 Pa. Therefore, an appropriate structure can achieve the dual benefits of enhanced heat exchange and reduced pressure loss. Moreover, the pressure loss, Q_l, Q_s, Q_t, and flue gas flow rate all showed a linear trend within 6000~13000 m^3/h within the three DPHEs, providing a particular direction for predicting other gas-liquid DPHE performance parameters of the same type. Significant differences in pressure and temperature distributions cause a more extensive distribution of condensate within 3rd DPHE, and the resulting film flow of condensate also alters the heat transfer process, leading to an excellent performance. In summary, the 3rd DPHE possesses the strongest heat exchange capacity and the lowest pressure loss, which requires an appropriate structure to generate turbulence conducive to heat exchange.

4.2. Overall performance evaluation of DPHEs

Based on previous studies [23,41–43], the criterion of the *Nu* to Re for DPHE can be expressed in the form of Eq. (15) and Fig. 5(a). In general, for the heated fluid $n = 0.4$ and the cooled fluid $n = 0.3$, u_f and u_w are the fluid dynamic viscosity corresponding to fluid temperature and wall temperature. Establishing a heat exchange model for novel DPHE requires obtaining *C* and *m* from a large amount of experimental data. A dimensionless relation for the flow heat transfer on the flue gas side is derived as follows. Temperature of flue gas decreased from 348 to 303 K based on the tested data. Therefore, the average temperature of 325 K is taken as the characteristic temperature. According to the mathematical model fitted by former scholars, the Pr of flue gas at this characteristic temperature is 0.74, and the (u_f/u_w)^0.14 is 1.02. On this basis, determine *C* and *m* for the three DPHEs according to the fitting results. As shown in Eq. (16), the *C* of 1st DPHE is 1.95, and *m* is 0.4276; the *C* and *m* of 2nd DPHE are 0.016 and 1.038, respectively. The *C* and *m* of the 3rd DPHE were 0.75 and 0.5825, respectively. It can be seen that 1st and 3rd DPHE have similar *C* and *m*, while 2nd DPHE has a completely different *C* and *m*, which proves that different foundation plate types determine the *C* and *m* of the fitting formula. *m* reflects the heat transfer performance of the heat exchanger, and the larger *m* corresponds to the better heat transfer capacity. 3rd DPHE has the best heat transfer performance when Re is 4400 corresponding to *Nu* of 100. Table 5 gives the studies on flue gas recovery and some new DPHEs in the last three years. For comparison, Re = 2100 and 4500 are used as comparison points. Since the minimum Re of 3rd DPHE is 2400, but based on the trend change, it can be inferred that the *Nu* is about 65 at Re = 2100. Comparisons of literature [15,19,22,23] fully prove that the 3rd DPHE proposed in this work has more excellent heat transfer performance.

In addition to heat transfer performance, pressure loss is a crucial indicator of DPHE. The resistance encountered by the fluid in the flow process mainly includes friction and local resistance. The focus of the DPHE resistance experiment in this paper is to obtain the influence of different geometric designs on the resistance, mainly considering friction resistance. Fanning friction factor (*f*) is used to evaluate the fluid flow performance, and the lower value indicates better fluid flow performance. The form of Fanning friction factor criterion equation was summarized by previous scholars as shown in Eq. (15). Dimensionless correlations of the resistance of the three DPHEs were obtained by fitting analysis in Eq. (17). *f* decreases with an increase in flue gas flow rate for both 2nd and 3rd DPHE in Fig. 5(b). Although the pressure drop of the fluid increases with increasing flow rate, the average velocity of the fluid

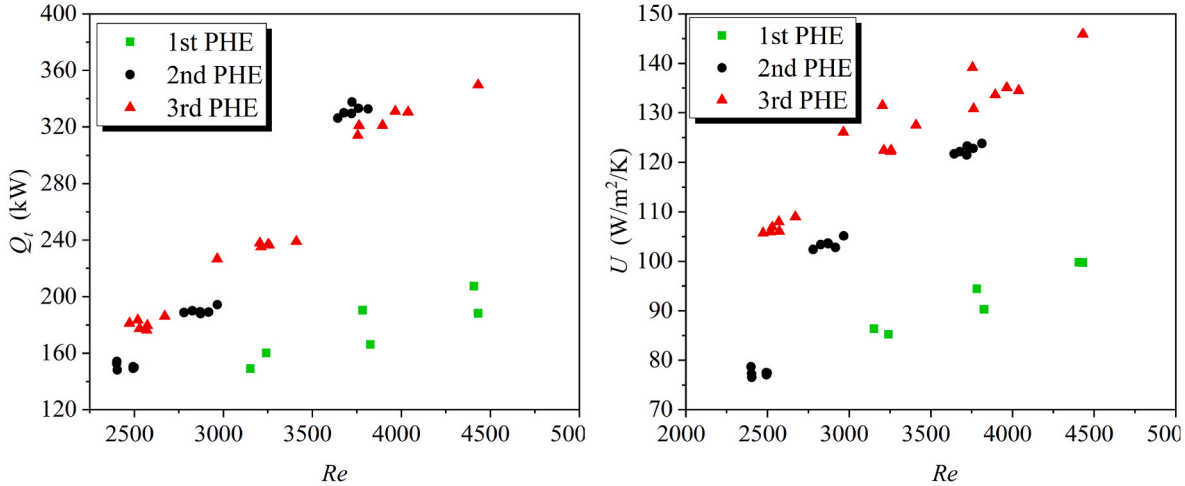

Fig. 6. *Re*-Q_t dimensionless relationship of three DPHEs and the comparison dimensionless relationship of *Re*-*U*.

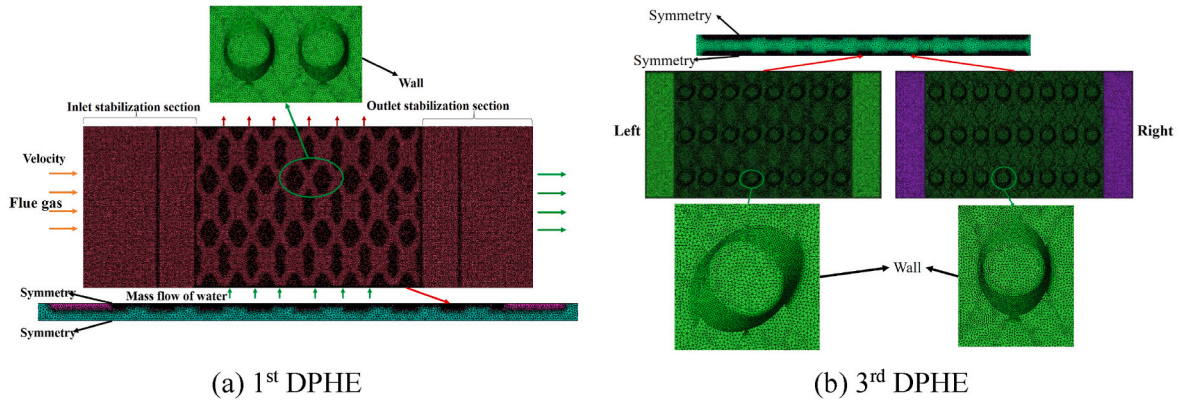

Fig. 7. Grid meshing and boundary conditions of 1st and 3rd DPHE.

increases significantly at the same time, resulting in a gradual decrease in f. Change in the f of both 2nd and 3rd indicates that the fluid flow performance increases with the increase of the fluid mass flow rate, but the enhancement effect decreases gradually. f of 1st DPHE remains almost constant with increasing flow rate, indicating that the fluid flow performance does not improve with increasing flow rate. In the transition region ($2000 < Re < 4000$), the flow state gradually shifts from laminar to turbulent, and the fluid behavior becomes unstable, characterized by both laminar features and turbulent disturbances. This results in more complex variations in the friction factor, which cannot be described by a simple formula. The design of 1st DPHE may lead to more pronounced flow irregularities or transitional phenomena. Fluid behavior becomes unstable, exhibiting both laminar characteristics and turbulent disturbances. As a result, the variation in the friction factor becomes more complex. The author believes 1st DPHE performs the worst due to higher pressure losses and poorer heat exchange. Overall, the dimensionless correlations of heat transfer and pressure loss of three novel gas-liquid DPHEs are obtained, which have a theoretical guiding significance for condensation-involving DPHE.

$$Nu = C\mathrm{Re}^{m}\,\mathrm{Pr}^{n}\left(\frac{\mu_f}{\mu_w}\right)^{0.14} \qquad f = BRe^{h} \tag{15}$$

Fig. 6 (b), the U increases with the rise in flue gas flow rate, consistent with the conclusions of Zhou et al. [44]. Although the U of 2nd DPHE is smaller than that of 3rd DPHE, the Q_t of the two DPHEs is close because the heat transfer area of 2nd DPHE is larger than that of 3rd DPHE. Given a smaller U and heat transfer area, 1st DPHE has the minimum Q_t. Additionally, there is a slight flat stage in the later stage, indicating that the U of the three DPHEs shows a linear trend within the range of design conditions. As the flow rate increases, the U of the 3rd DPHE can reach about 150W/(m^2·K), followed by the 2nd and 1st DPHE. To sum up, the 3rd DPHE has the best heat transfer and pressure loss performance based on comparing U, Q_t and f. Considering the 3rd DPHE is a modification of 1st DPHE, the next focus is to analyze the heat transfer mechanism of 3rd DPHE and provide direction for subsequent optimization of DPHE.

4.3. Modeling and simulation verification of 1st DPHE and 3rd DPHE

Comparisons of critical indicators confirmed that the heat transfer and pressure loss performance of the 3rd DPHE has been significantly improved by twisting one side of the dimples to 45°. Understanding the fundamental mechanisms is the basis for optimizing the internal structure of DPHEs. Therefore, 1st and 3rd DPHEs are modeled and meshed in this study to identify synergistic enhancement mechanisms through the results of CFD. Fig. 7 displays the three-dimensional models and mesh diagrams of the 1st and 3rd DPHEs, respectively. Since the shapes of the left and right plates of 1st DPHE are identical, this work only completed the modeling of half of the internal flow channel structure and set some of the wall surfaces as symmetrical boundaries to reduce the computational workload. Due to the asymmetry between the left and right sides of the plates in 3rd DPHE, it was necessary to complete the modeling of the entire internal flow channel structure. Mathematical and physical boundary conditions of the internal flow channel structures of 1st and 3rd DPHE are shown in Fig. 7. Numerical calculations have been performed in this paper using Ansys Fluent 2022R1 according to several scholars. Specific control equations are referencing to Duan et al. [19] being given below, Eq. (18)–(29). In the governing equations, **u** and T denote the vector velocities and temperatures of the different phases in

$$\begin{aligned}
Nu_{(1stPHE)} &= 1.95\mathrm{Re}^{0.4276}\,\mathrm{Pr}^{0.3}\left(\frac{\mu_f}{\mu_w}\right)^{0.14}\left\{3000 < \mathrm{Re} < 5000, 0.73 < \mathrm{Pr} < 0.74, 1.0 < \frac{\mu_f}{\mu_w} < 1.1\right\}\\
Nu_{(2ndPHE)} &= 0.016\mathrm{Re}^{1.038}\,\mathrm{Pr}^{0.3}\left(\frac{\mu_f}{\mu_w}\right)^{0.14}\left\{2000 < \mathrm{Re} < 4000, 0.73 < \mathrm{Pr} < 0.74, 1.0 < \frac{\mu_f}{\mu_w} < 1.1\right\}\\
Nu_{(3rdPHE)} &= 0.75\mathrm{Re}^{0.5825}\,\mathrm{Pr}^{0.3}\left(\frac{\mu_f}{\mu_w}\right)^{0.14}\left\{2000 < \mathrm{Re} < 5000, 0.73 < \mathrm{Pr} < 0.74, 1.0 < \frac{\mu_f}{\mu_w} < 1.1\right\}
\end{aligned} \tag{16}$$

$$\begin{aligned}
f_{(1stPHE)} &= 0.34\mathrm{Re}^{0.083}\{3000 < \mathrm{Re} < 5000\}\\
f_{(2ndPHE)} &= 78.77\mathrm{Re}^{-0.61}\{2000 < \mathrm{Re} < 4000\}\\
f_{(3rdPHE)} &= 46.01\mathrm{Re}^{-0.54}\{2000 < \mathrm{Re} < 5000\}
\end{aligned} \tag{17}$$

Fig. 6 (a) shows the variation trend of Q_t with Re increased for three DPHEs, which shows an approximately linear trend with the increasing Re. The increase in flue gas flow rate enhances the heat dissipation capacity. At the same time, the shorter residence time of the flue gas in the DPHE increases the temperature difference for heat exchange with cold water, leading to improved heat transfer performance. Combined with

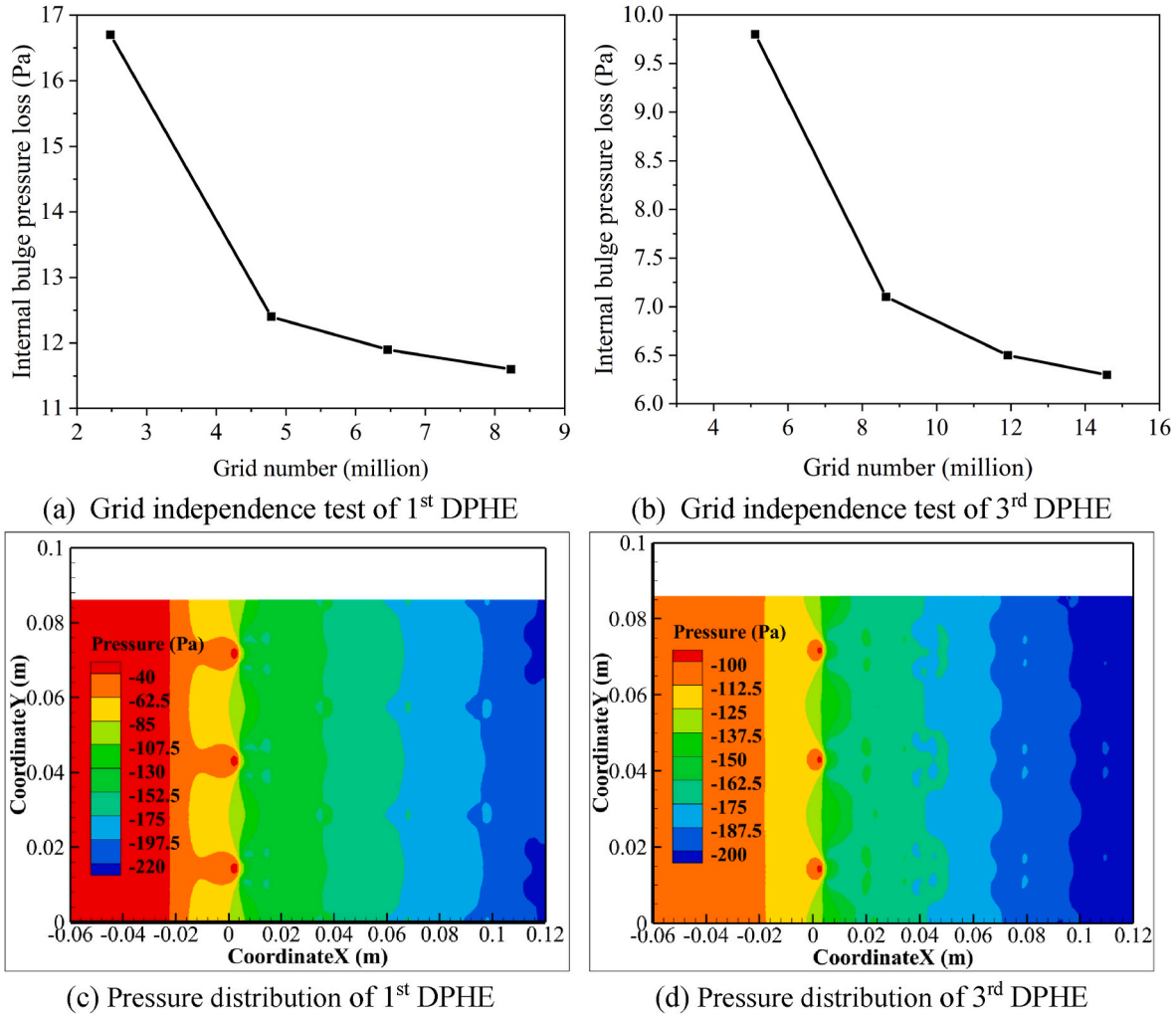

Fig. 8. Grid independence test and pressure distribution of 1st and 3rd DPHE.

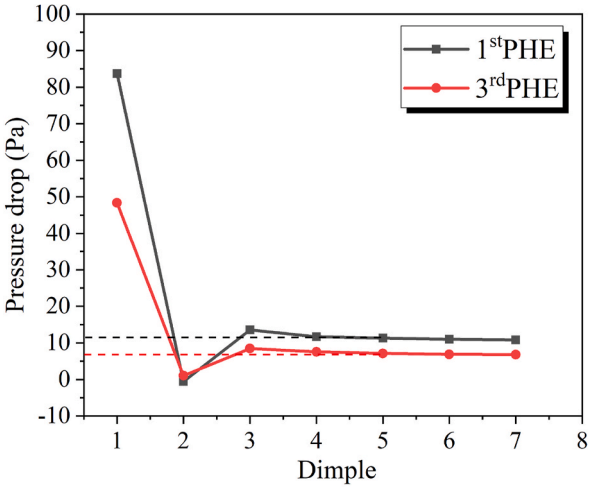

Fig. 9. Pressure loss caused by each dimple of 1st and 3rd DPHE.

Table 6
Simulation condition table.

Working condition	DPHE	Waterside flow (kg/s)	Flue gas side flow (m/s)	Waterside full state
Case 1	1st DPHE	0.12	4.05	Sufficient
Case 2	1st DPHE	0.12	5.2	Sufficient
Case 3	1st DPHE	0.0033	4.05	Insufficient
Case 4	1st DPHE	0.0033	5.2	Insufficient
Case 5	3rd DPHE	0.12	4.05	Sufficient
Case 6	3rd DPHE	0.12	5.2	Sufficient
Case 7	3rd DPHE	0.0033	4.05	Insufficient
Case 8	3rd DPHE	0.0033	5.2	Insufficient

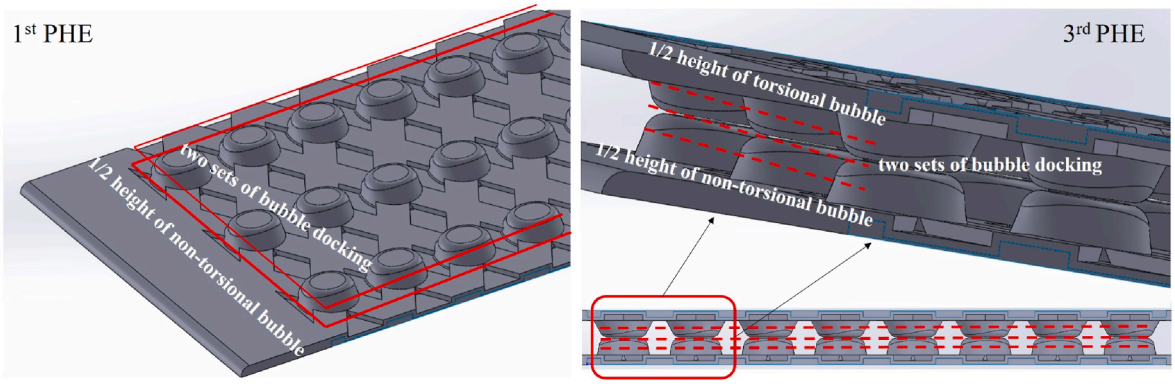

Fig. 10. Schematic diagram of the studied section selection.

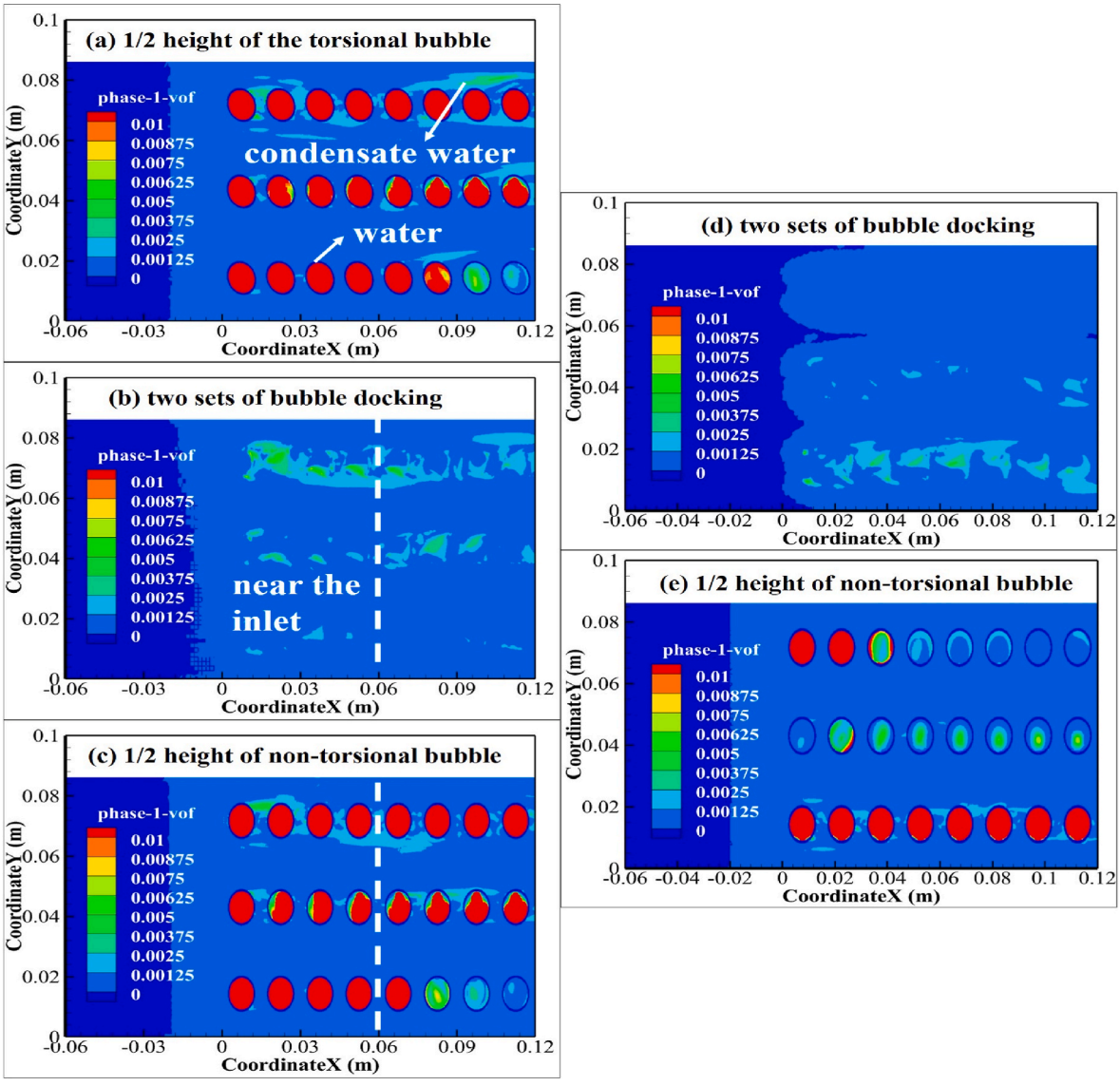

Fig. 11. Volume fraction distribution of condensate water of case 7 [3rd DPHE:(a)(b)(c)] and case 3 [1st DPHE:(d)(e)].

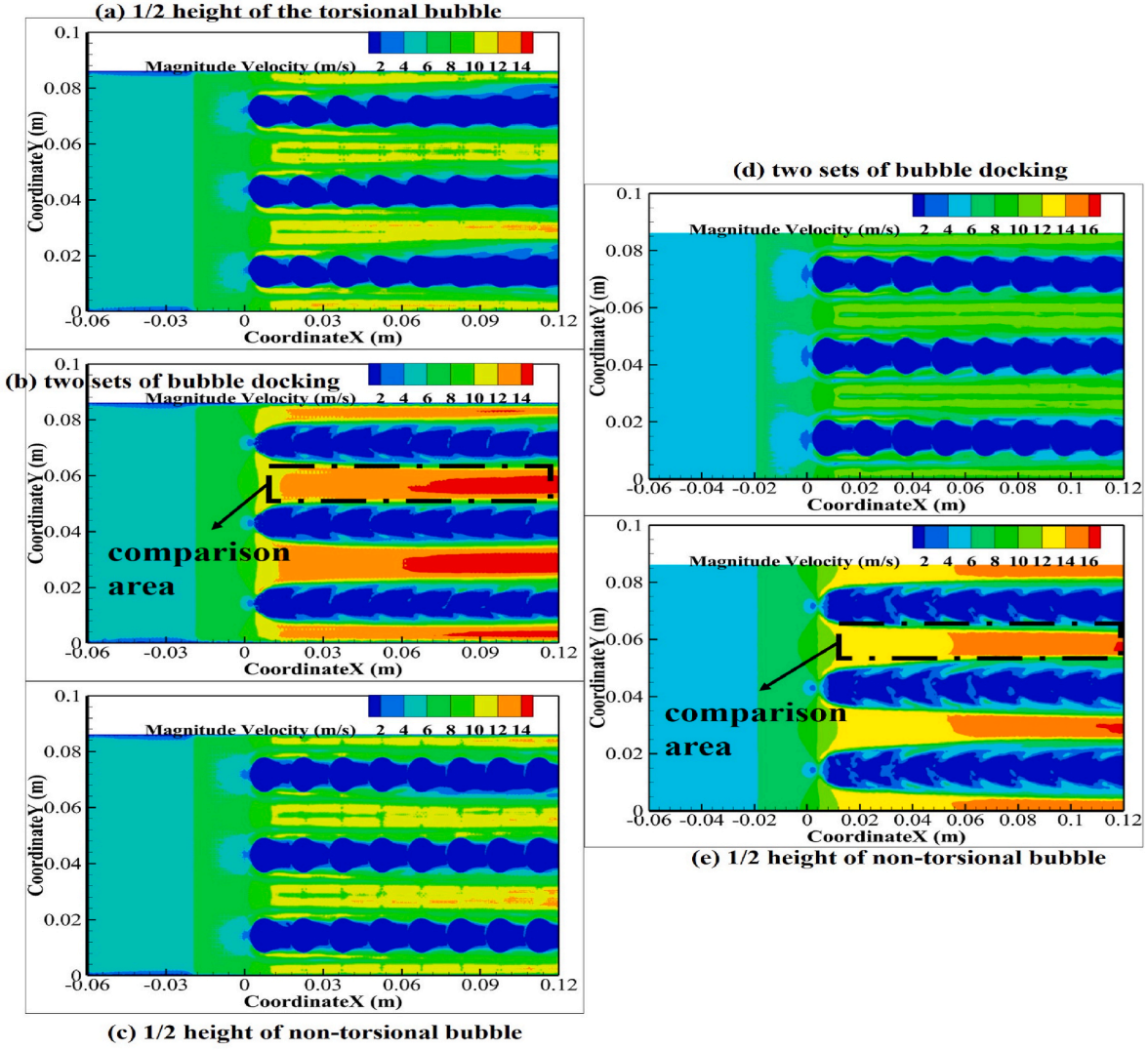

Fig. 12. Velocity distribution of case 7 [3rd DPHE:(a)(b)(c)] and case 3 [1st DPHE:(d)(e)].

the computational cell, respectively, C_p is the specific heat of the different phases in the computational cell, λ is the effective thermal conductivity, $\mathbf{g}$ is the gravitational acceleration, τ is the shear stress, P denotes the pressure, and S denotes the source of additional mass for the interphase transformation. In the flue gas-steam-water momentum equation, $\mathbf{F}$ denotes the interfacial force between the different phases. In the flue gas-steam-water energy equation, q denotes the heat source transferred between the different phases. The most classical k-ε equation was chosen for the turbulence model and will not be repeated here.

Continuity equation for the flue gas phase:

$$\frac{\partial(\alpha_f\rho_f)}{\partial t}+\nabla\cdot(\alpha_f\rho_f\mathbf{u}_f)=0 \tag{18}$$

Momentum equation for the flue gas phase:

$$\frac{\partial(\alpha_f\rho_f\mathbf{u}_f)}{\partial t}+\nabla\cdot(\alpha_f\rho_f\mathbf{u}_f\mathbf{u}_f)=-\alpha_f\nabla P+\alpha_f\rho_f\mathbf{g}+\nabla\cdot(\alpha_f\tau_f)+\mathbf{F}_f \tag{19}$$

The energy equation for the flue gas phase:

$$\frac{\partial(\rho_f c_{p,f}T_f)}{\partial t}+\nabla\cdot(\alpha_f\rho_f\mathbf{u}_f c_{p,f}T_f)=\nabla\cdot(\alpha_f\lambda_f\nabla T_f)+\left(q_f\right) \tag{20}$$

Continuity equation for the vapor phase:

$$\frac{\partial(\alpha_{vap}\rho_{vap})}{\partial t}+\nabla\cdot(\alpha_{vap}\rho_{vap}\mathbf{u}_{vap})=S_{vap-con} \tag{21}$$

Momentum equation for the vapor phase:

$$\frac{\partial(\alpha_{vap}\rho_{vap}\mathbf{u}_{vap})}{\partial t}+\nabla\cdot(\alpha_{vap}\rho_{vap}\mathbf{u}_{vap}\mathbf{u}_{vap})=-\alpha_{vap}\nabla P+\alpha_{vap}\rho_{vap}\mathbf{g}+\nabla\cdot(\alpha_{vap}\tau_{vap})+\mathbf{F}_{vap} \tag{22}$$

The energy equation for the vapor phase:

$$\frac{\partial(\rho_{vap}c_{p,vap}T_{vap})}{\partial t}+\nabla\cdot(\alpha_{vap}\rho_{vap}\mathbf{u}_{vap}c_{p,vap}T_{vap})=\nabla\cdot(\alpha_{vap}\lambda_{vap}\nabla T_{vap})+\left(q_{vap}\right) \tag{23}$$

Continuity equation for the condensate phase:

$$\frac{\partial(\alpha_{con}\rho_{con})}{\partial t}+\nabla\cdot(\alpha_{con}\rho_{con}\mathbf{u}_{con})=S_{con-vap} \tag{24}$$

Momentum equation for the condensate phase:

$$\frac{\partial(\alpha_{con}\rho_{con}\mathbf{u}_{con})}{\partial t}+\nabla\cdot(\alpha_{con}\rho_{con}\mathbf{u}_{con}\mathbf{u}_{con})=-\alpha_{con}\nabla P+\alpha_{con}\rho_{con}\mathbf{g}+\nabla\cdot(\alpha_{con}\tau_{con})+\mathbf{F}_{con} \tag{25}$$

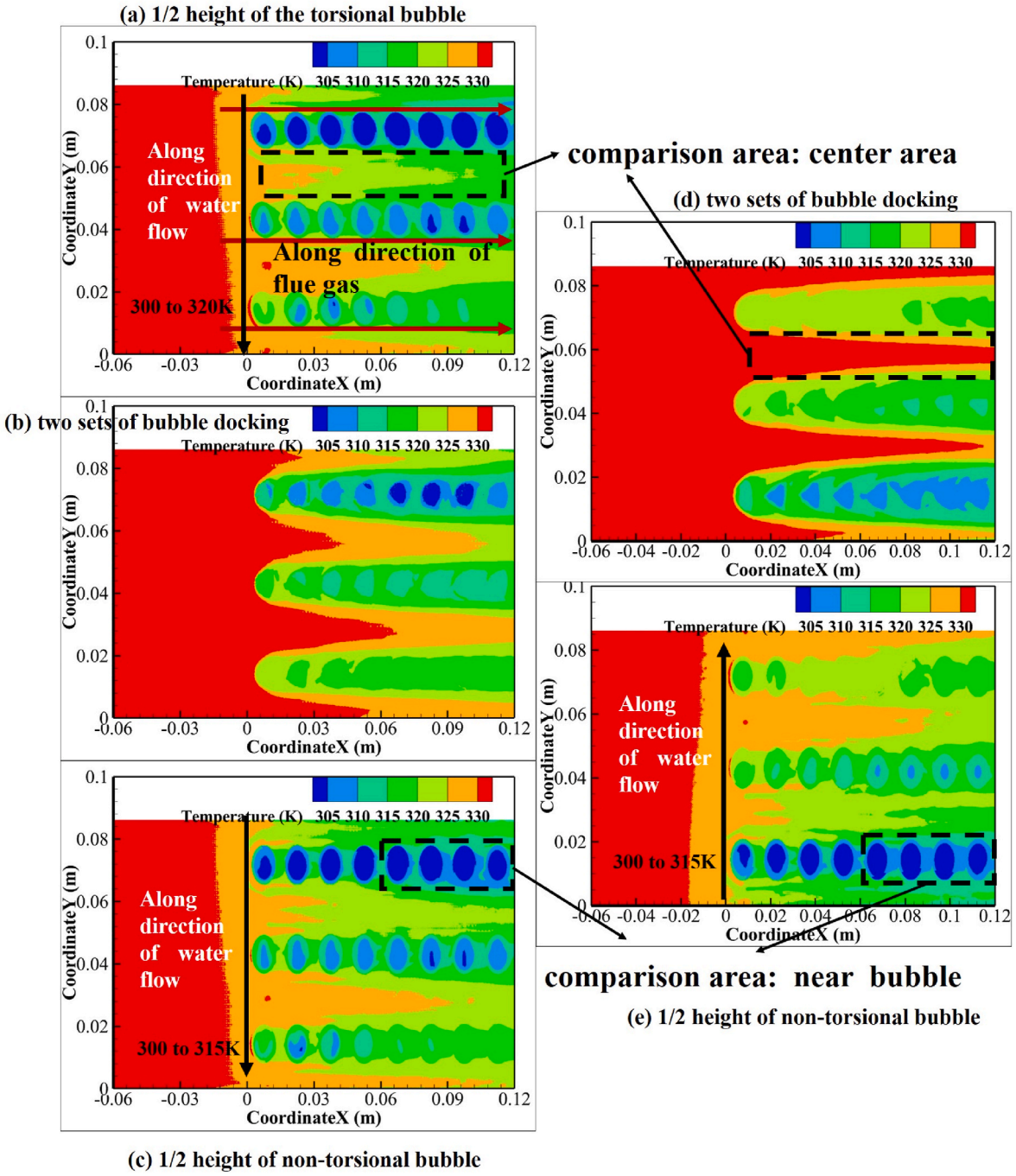

Fig. 13. Temperature distribution of case 7[3rd DPHE:(a)(b)(c)] and case 3 [1st DPHE:(d)(e)].

The energy equation for the condensate phase:

$$\frac{\partial(\rho_{con}c_{p,con}T_{con})}{\partial t}+\nabla\cdot(\alpha_{con}\rho_{con}\mathbf{u}_{con}c_{p,con}T_{con})=\nabla\cdot(\alpha_{con}\lambda_{con}\nabla T_{con})+(q_{con}) \tag{26}$$

Interfacial heat transfer

$$q_{vap}=\frac{h_{vap-f}a_{if,vap}(T_{vap}-T_f)}{\alpha_{vap}} \tag{27}$$

$$q_{con}=\frac{h_{con-f}a_{if,con}(T_{con}-T_f)}{\alpha_{con}} \tag{28}$$

$$q_f=\left(-q_{vap}-q_{con}\right) \tag{29}$$

Velocity and pressure fields are solved based on momentum and Poisson; (2) The velocity field is corrected to satisfy the continuity equation based on the pressure field, and the corrected velocity field needs to be re-started in the first step of the cycle if it still does not satisfy the continuity equation; (3) After the loop iterations converge, Tablethe energy, turbulence, and component transport equations are solved within the SIMPLE algorithm. “Velocity” and “mass inlet” boundary conditions were used for flue gas (hot side) and water (cold side), which is mainly because flue gas velocity and water mass flow rate were measured during the test. The outlet boundary conditions for the hot and cold sides were set as “outflow”. The upper and lower surfaces of the

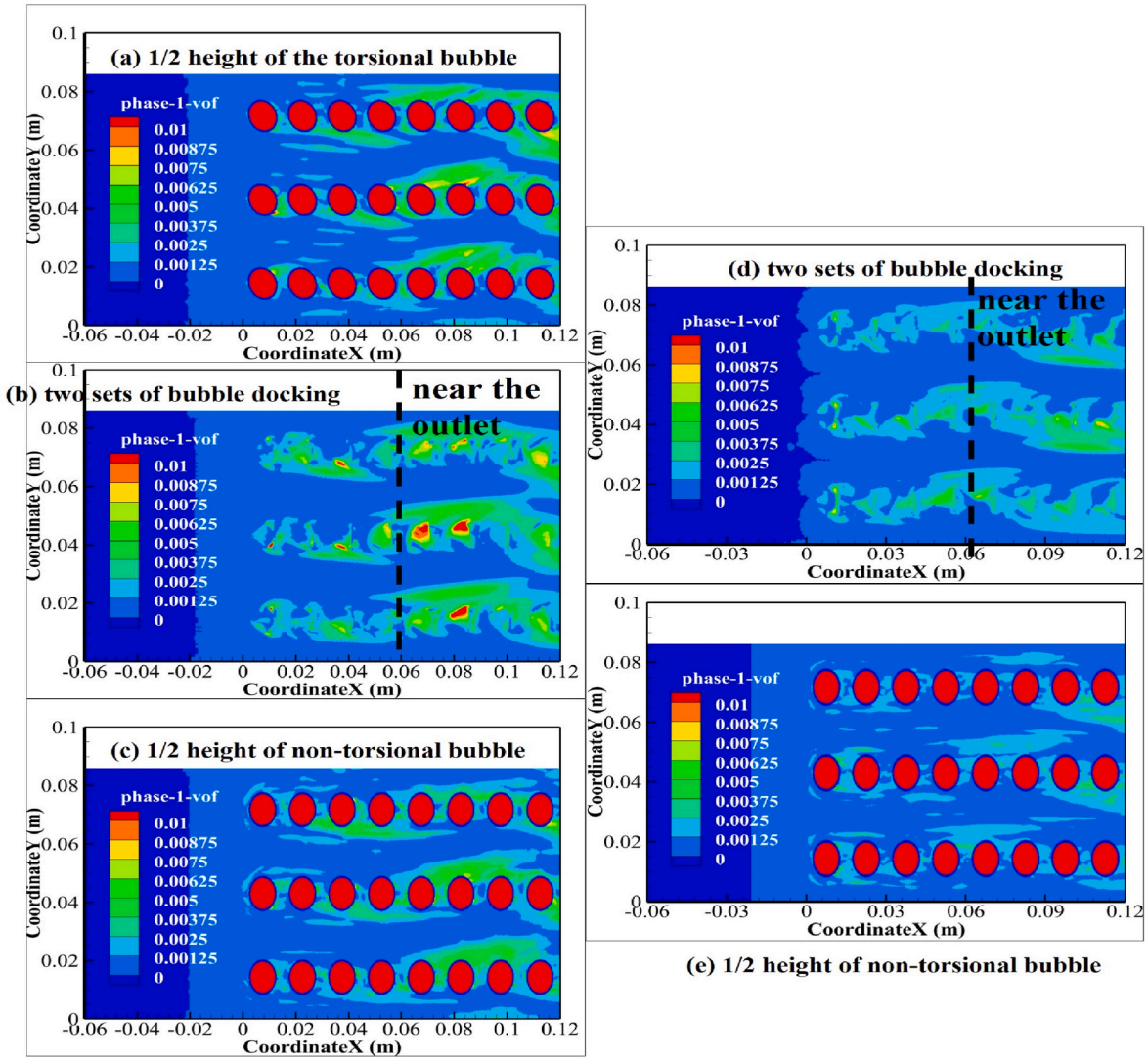

Fig. 14. Volume fraction distribution of condensate water of case 5 [3rd DPHE:(a)(b)(c)] and case 1 [1st DPHE:(d)(e)].

computational domain are "symmetric" boundary conditions to reduce the computational effort. The rest of the surfaces are set as wall conditions with momentum and heat boundary conditions "no slip" and "system coupling". The mathematical forms of the continuity, momentum, and energy boundary conditions for the flue gas inlet, water inlet, outlet, heat exchanger wall, and symmetry plane are as show in Eq. (30)–(34). Each equation is divided into three parts, with the boundary conditions for continuity, momentum, and energy equations presented from left to right.

Flue gas inlet: Velocity Inlet

$$\mathbf{u} = \mathbf{u}_{in}, T = T_{in} \tag{30}$$

Water inlet: Mass Inlet

$$\rho \mathbf{u} \cdot \hat{n} = \dot{m}, \mathbf{u} = \frac{\dot{m}}{\rho}\hat{n}, T = T_{in} \tag{31}$$

Outlet: Outflow

$$\mathbf{u} \cdot \hat{n} = 0, \frac{\partial T}{\partial n} = 0 \tag{32}$$

Heat exchanger wall: Wall

$$\mathbf{u} = 0, \frac{\partial T}{\partial n} = 0 \tag{33}$$

Symmetry plane: Symmetric

$$\mathbf{u} \cdot \hat{n} = 0, \frac{\partial T}{\partial n} = 0 \tag{34}$$

Pressure loss of the internal dimple of the DPHE is used as test variable for mesh independence. It can be seen from Fig. 8 (a)(b) that the pressure loss of the 1st DPHE is stabilized at 11.5 Pa when the number of grids is 8 million, and the pressure loss of the 3rd DPHE is stabilized at 6.3 Pa when the grid is 14 million. Therefore, 8 million grids and 14 million grids are finally selected for numerical calculations to save computational resources. This study conducted simulations for 1st and 3rd DPHE under case 1 to ensure the accuracy of the CFD calculations, with the pressure distribution cloud diagrams shown in Fig. 8. In the experiments, the 1st and the 3rd DPHE were divided into 4 flow sections, each containing 8 rows of dimples. This study only simulated one section that includes 8 rows of dimples to save computational resources. It can be observed from Fig. 8 (c)(d) that the row of dimples at the inlet has the highest pressure loss, while the subsequent dimples experience less pressure loss, which is an issue worth noting. Furthermore, it can be hypothesized that modifying only the dimples at the inlet could reduce the pressure loss of the heat exchanger. It is necessary to get the average pressure loss of each internal dimple to obtain the pressure loss of the whole DPHE. As shown in Fig. 9, the pressure loss of each dimple inside the 1st DPHE is 11.6 Pa and the inlet dimple is 84 Pa. Pressure loss of

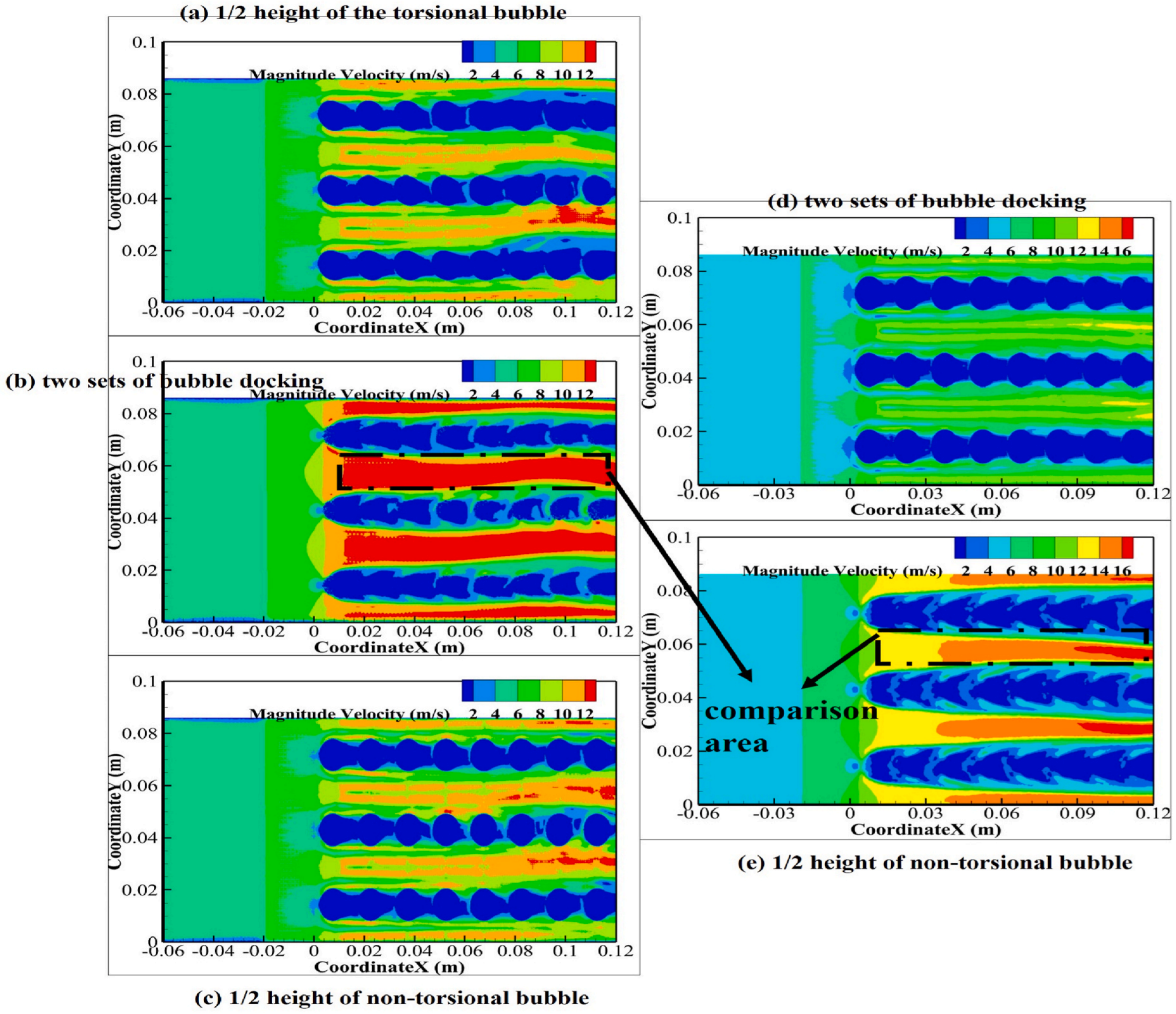

Fig. 15. Flow field distribution of case 5 [3rd DPHE:(a)(b)(c)] and case 1 [1st DPHE:(d)(e)].

each dimple of the 3rd DPHE is 6.3 Pa and the inlet dimple is 48 Pa. Simulated DPHE pressure loss can be obtained by multiplying the internal 31 dimples and adding a dimple pressure loss at the inlet, which of the 1st DPHE is 443.6 Pa and the experimental value is 447 Pa with relative error is less than 1 %. Simulation value of the 3rd DPHE is 243.3 Pa and the experimental value is 220 Pa, with a relative error is 10 %. Both sets of comparative results fully prove the accuracy of the numerical simulation. Subsequently, this study simulates the thermal-fluid behavior under eight cases for both DPHEs, as shown in Table 6. Flue gas inlet temperature was 333 K and the cold water inlet was 300 K.

4.4. Analysis and comparison of simulation results of 1st DPHE and 3rd DPHE

It is evident that Q_l accounts for 30–50 % of Q_t from the above experimental data, and the primary source of the gap between the 1st and 3rd DPHE is Q_l. Therefore, the phase change process of vapor must be considered in CFD calculation. In this work, the User-Defined Function (UDF) is implanted into Fluent to complete calculations and monitoring of vapor condensation. Specific realization steps are as follows: (1) Obtain the calculation domain number of the main phase flue gas and traverse each grid unit to obtain the temperature and pressure; (2) Based on the model of Lee et al. [45], the specific parameter in Eq. (35) was used to determine whether the grid unit is condensed and the condensation amount; (3) Condensation mass and energy are transferred to the secondary phase (water). Complex flow channel structure within the DPHE can result in significant differences in flow and heat transfer parameters, even in small spatial proximities. Therefore, multiple locations need to be selected for cloud analysis. Fig. 10 shows two and three cross-sections were selected in 1st and 3rd DPHE to investigate the flow, temperature, and condensate distribution field, respectively. Fig. 11 shows the condensate volume fraction of 1st and 3rd DPHE and finds some dimples that are not filled with water due to the small flow rate on the waterside. Condensate primarily accumulates around the twisted dimples and flue gas inlets. In addition, the condensate distribution of 1st DPHE is less than that of 3rd DPHE. Dimple torsion can make the waterside flow more uniform, and most of the dimples contain water under the same flow rate by comparing (c) and (e), which provides a larger cooling surface area. Similarly, Fig. 12 compares the flow field distribution of the two DPHEs; the flue gas velocity of the 3rd DPHE is lower at the same flow rate. As can be seen from (b) and (e), flue gas velocity is about 13~15 m/s in the middle region within the 1st DPHE and is about 12~14 m/s within the 3rd DPHE, which also provides favorable conditions for the full heat exchange between the flue gas and water. Uniform flow on the waterside and sufficient internal heat transfer time are the main reasons for the enhanced effect caused by the torsion of the dimple angle.

$$S_{vap-con} = r\alpha_{vap}\rho_{vap}\frac{(T_{sat} - T_{vap})}{T_{sat}} \quad S_{con-vap} = r\alpha_{con}\rho_{con}\frac{(T_{con} - T_{sat})}{T_{sat}} \tag{35}$$

Temperature field of the 3rd DPHE is lower than that of the 1st DPHE, which shows comparisons in Fig. 13. Taking the docking place of

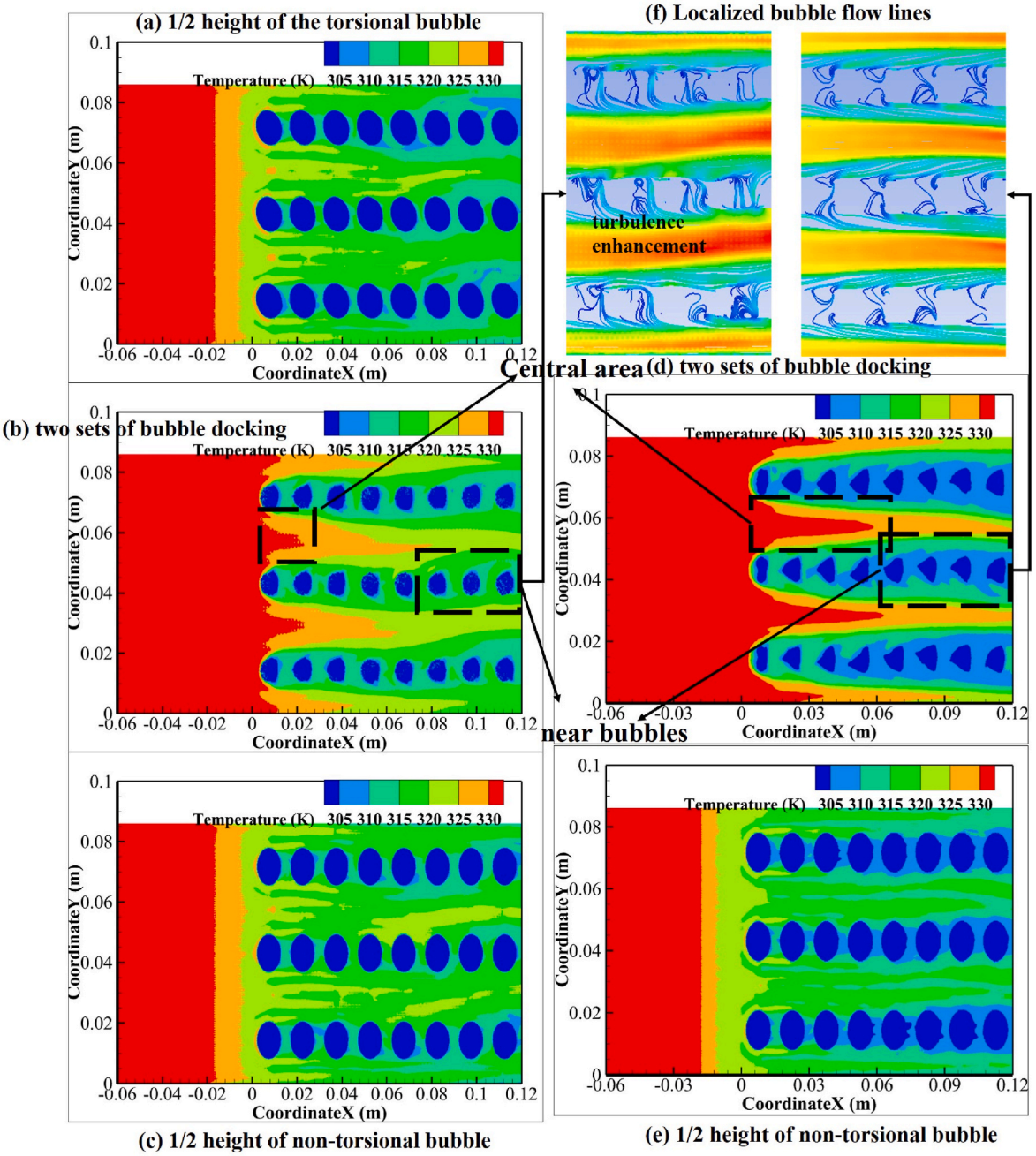

Fig. 16. Temperature field distribution of case 5 [3rd DPHE:(a)(b)(c)] and case 1 [1st DPHE:(d)(e)].

the two sets of dimples as an example, there is still a high-temperature region of 330 K in the 1st DPHE after the high-temperature flue gas flows through 8 sets of dimples. However, the high-temperature flue gas flows through 4 sets of dimples and drops to below 325 K in the 3rd DPHE. In addition, by comparing the black box lines in Fig. 13 (c)(e), the flue gas temperature drop near the dimples is more obvious in 1st DPHE but is not significant enough compared to the 3rd DPHE in the center area. This phenomenon confirms that the corrugations in 1st DPHE cannot generate significant turbulence, thus failing to facilitate heat exchange between the flue gas around the dimples and the cold medium. Three sets of horizontally oriented dimples have different water content, resulting in a significant temperature difference between the flue gas after heat exchange shown in Fig. 13(a). When the water quantity is sufficient, the flue gas temperature can be reduced from 330 K to 310 K, a decrease of 20 K; when the water quantity is insufficient, the flue gas temperature decreases from 330 K to 315 K, a decrease of 15 K. Based on the black arrows in Fig. 13(a)(c), it is evident that the cold water temperature increases from 300 K to 320 K for a 45° twisted dimple and from 300 K to 315 K for a non-twisted dimple. Fig. 13(e) demonstrates the cold water temperature at the dimple increasing from 300 K to 315 K, which is consistent with the non-twisted dimple in Fig. 13(a).

Flow heat transfer in the state of insufficient flow was analyzed above, and the enhanced mechanism of the 3rd DPHE was clarified. Subsequently, the distribution of condensed water, flow rate and temperature field of 3rd and 1st DPHE are analyzed when the waterside flow is sufficient. The amount of condensate water in the 3rd DPHE is increased obviously by comparing Figs. 14 and 11. Area of condensate water is close to the backside, which is different from the insufficient flow on the waterside. This phenomenon is due to the fact that all dimples are filled with water, and the flue gas temperature gradually

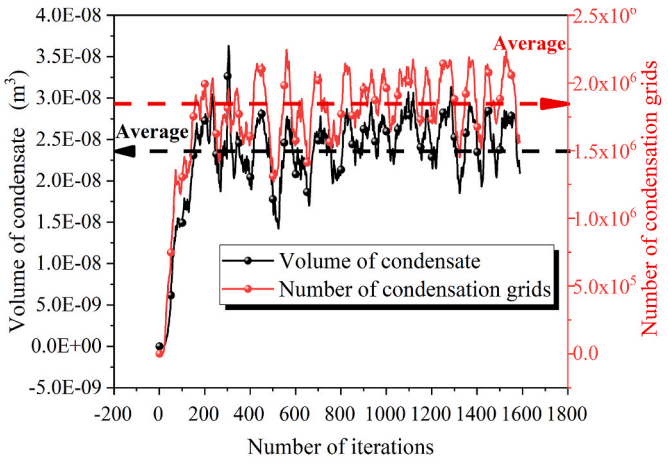

Fig. 17. The changing trend of the proportion of the condensed water grid and the total amount of condensed water with the number of iteration steps.

decreases as the flow deepens, resulting in more condensed water in the backside. By comparing the flow field shown in Fig. 15(b)(e), the torsion of 3rd PHE causes the flue gas velocity to decrease significantly in the center area of the channel, about 2 m/s, which will lead to more sufficient heat transfer of flue gas. In addition, the flow in the black box, as shown in Fig. 15(b), is more unstable and the low-flow region near the dimples is smaller compared to that in Fig. 15(e).

As shown in Fig. 16, the temperature field distribution of 3rd DPHE is lower than that of 1st DPHE. Taking the two sets of dimple docking as an example, the temperature can be reduced to 325 K through 2 dimples from the inlet of 3rd DPHE. Meanwhile, the temperature was reduced to 325 K in the 1st DPHE through 4–5 dimples from the entrance. However, flue gas temperature drops around the 1st DPHE dimple are more significant than the 3rd DPHE based on comparing the black boxes in Fig. 16(b)(d), which is consistent with the above study. The difference in heat transfer between the central area of the flue gas and near the dimples is due to the twisting of the dimples in the flow channel of the 3rd DPHE, which expands the spatial dimensions of turbulence with achieving a larger heat transfer surface area as shown in Fig. 16(f). Larger turbulence transfers the cold to the intermediate region, resulting in a greater reduction in the central area but less near the dimples.

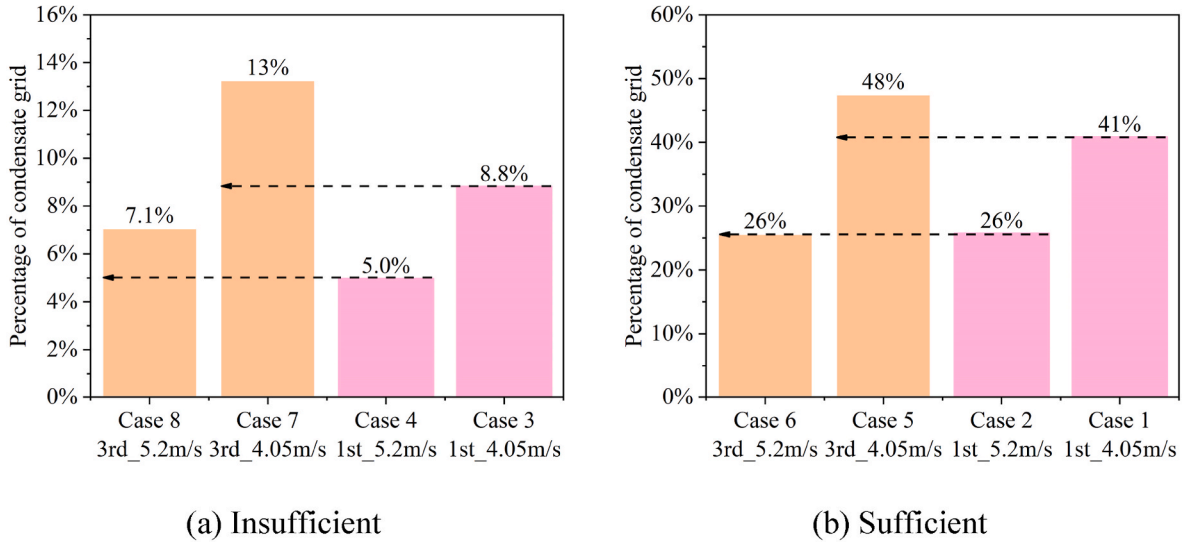

Fig. 18. Comparative analysis of the proportion of condensate water grid.

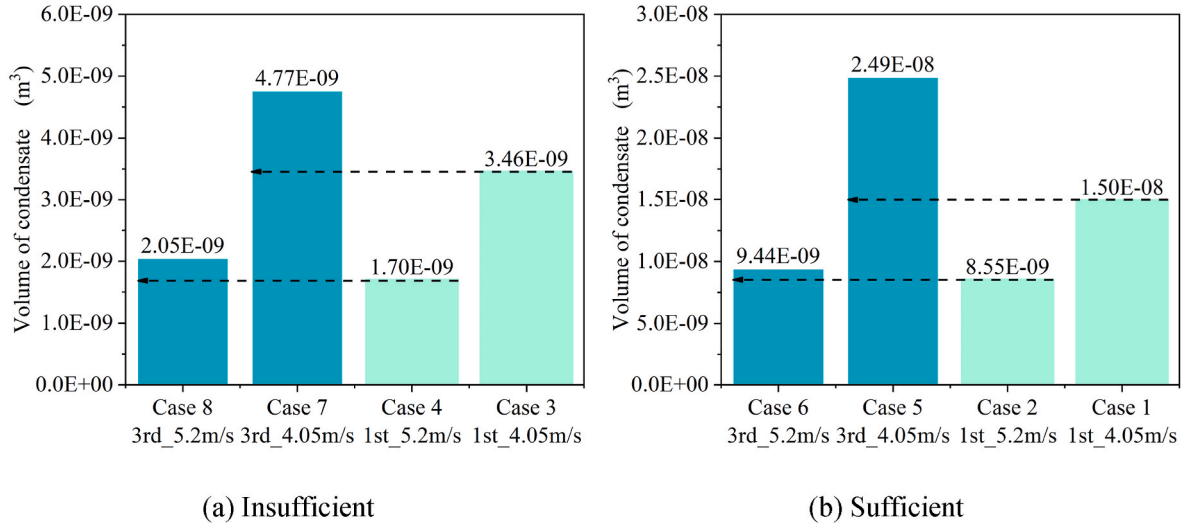

Fig. 19. Comparative analysis of condensation water.

Therefore, the twisting dimples first cause changes in the internal flow field distribution within the flue gas, resulting in sufficient heat transfer between the flue gas and the water side. Subsequently, the temperature field of the flue gas undergoes significant changes, ultimately leading to a significant increase in the amount of condensate water within the plate and enhancing the heat transfer capacity from both sensible and latent heat perspectives.

4.5. Analysis of improved lifting mechanism

In the above chapter, the macroscopic principle that the heat transfer performance of 3rd DPHE is better than that of 1st DPHE is clarified in terms of the flow velocity, condensate distribution, and temperature field distribution. Furthermore, the proportion of internal condensate grids and the total condensate volume of the two DPHEs were statistically analyzed to explain the mechanism of heat transfer performance improvement from a microscopic perspective. Fig. 17 shows the variation trend of the total number of grids and the volume of condensate with iteration steps in case 7. Two parameters are in a stable state of dynamic fluctuation in the later period. Therefore, the eight groups of cases in Table 2 are set up with 2000 iteration steps, and the average value of the next 500 iteration steps is taken as the comparison data. Fig. 18(a) is the proportion of the total grid of condensation water in cases 3,4,7 and 8, and Fig. 18(b) is the proportion of the grid of condensation water in cases 1,2,5 and 6. When the waterside is filled with cold water, the proportion of condensed water grids in DPHE (20–50 %) is much higher than waterside is not filled (4–14 %), which is consistent with the above cloud diagram. Proportion of condensed water grids in the low flow rate conditions of 1st and 3rd DPHE is twice that of the high flow rate conditions, indicating that the flow rate has an important influence on the distribution of condensed water and the proportion of latent heat of the two DPHEs. The proportion of condensation water grid in the 3rd DPHE is always higher than that in the 1st DPHE, especially at a low flue gas flow rate. Condensate water distribution of 3rd DPHE is wide, and the condensation area in DPHE is more extensive after twisting the dimple.

A more detailed analysis of the overall condensate volume also reveals that the total amount of condensate in the 3rd DPHE consistently exceeds that in 1st DPHE. It is worth noting that the increase in condensate volume requires two conditions: (1)the wide distribution of condensate or the increase of water film thickness, which corresponds to two different heat transfer mechanisms; (2)the wide distribution of condensed water indicates the structure changes the internal flow field and temperature field. Increasing water film thickness indicates that the heat transfer mode is film or bead, corresponding to two methods to enhance the heat transfer efficiency. As shown in Fig. 19, the changing trend of the condensate volume shows a high degree of agreement with number of condensate grids in Fig. 18, indicating that the wide distribution of condensate is the main reason why the condensate volume is higher than that of the 1st DPHE. It is further explained that the torsional dimple only changes the flow field distribution and does not change the heat transfer mechanism. In addition, there is no significant difference in the amount of condensation water between the two DPHEs under high-flow rate conditions, demonstrating the modified plate exchanger may have a more significant heat exchange advantage only in dealing with low-flow flue gas. The internal mechanism of the torsional dimple to enhance heat transfer was analyzed macroscopically by cloud diagram, and the main ways to enhance heat transfer were clarified based on the data. However, some problems remain to be solved, such as determining the most suitable angle for twisting the dimple, the optimal height, and the optimal dimple spacing. In the later stage, the dimple parameters of the optimal DPHE can be numerically calculated to achieve the dual improvement of pressure loss and heat transfer performance according to the established CFD model.

5. Conclusion

Gas-liquid DPHE is an effective instrument for recovering low-grade waste heat from flue gas, but the complex flow channel structure and condensation phenomenon make the development of new high-efficiency gas-liquid DPHE extremely difficult. In this work, three different types of DPHEs were tested on a pilot-scale experimental platform, and the performance of the DPHE was evaluated in terms of sensible and latent heat transfer capacity, flow pressure loss, and flow heat transfer coefficient. In addition, the flow and heat transfer state inside the two types of DPHEs were numerically simulated by CFD to clarify the heat transfer mechanism of this type of DPHE. Results show that (1) 3rd DPHE has optimal performance with total convective heat transfer coefficients up to 125 W/(m^2·K) at the tested flow rates. The lack of latent heat is the main reason for the poor performance of 2nd DPHE, where the latent heat, sensible heat, and pressure loss increase linearly with the flue gas flow rate; (2) *Re-Nu* and *Re-f* correlations for different types of DPHEs (with Re between 2000 and 5000) were obtained by fitting the experimental data, which fills the gap in flow heat transfer data for this type of DPHE; (3) Numerical simulations have determined that the first dimple at the inlet is the main source of pressure loss, accounting for about 20 % of the total pressure loss. Therefore, the pressure loss can be rapidly reduced by changing the form of the first dimple; (4) Macroscopic heat transfer mechanism of the modified DPHE (3rd DPHE) is clarified: the twisted dimple leads to a more uniform distribution of the water-side flow and expands the turbulence of flue gas, resulting in a full heat transfer. Afterward, the temperature field of flue gas drops significantly, which ultimately leads to a significant increase in the amount of condensate and enhances the heat transfer capacity from both sensible and latent heat levels; (5) Filling the cold side with water increases the flue gas side condensate distribution area by nearly one time (45 % vs 25 %) compared to unfilled water. Ability of the torsional dimple to increase latent heat transfer is primarily due to a broader condensable area rather than a change in heat transfer mode. Reducing the dimple spacing and adding a torsion angle is the optimal solution for increasing heat transfer efficiency and reducing pressure loss.

CRediT authorship contribution statement

Xiang Liu: Writing – review & editing, Writing – original draft, Visualization, Validation, Investigation, Formal analysis, Data curation. **Fengyongkang Wu:** Writing – review & editing, Formal analysis. **Xue Xue:** Writing – review & editing, Formal analysis. **Kelang Jin:** Writing – review & editing, Formal analysis. **Lei Zhang:** Writing – review & editing, Formal analysis. **Hao Zhou:** Project administration, Funding acquisition, Conceptualization.

Declaration of competing interest

The authors declare that they have no known competing financial interests or personal relationships that could have appeared to influence the work reported in this paper.

Acknowledgments

Supported by the Fundamental Research Funds for the Central Universities(2022ZFJH04)

Appendix A. Supplementary data

Supplementary data to this article can be found online at https://doi.org/10.1016/j.ijthermalsci.2025.109716.

Data availability

Data will be made available on request.

References

[1] Q. Ding, J. Huang, J. Chen, X. Luo, Climate warming, renewable energy consumption and rare earth market: evidence from the United States, Energy 290 (2024) 130276.

[2] M. Song, H. Zheng, Z. Shen, Whether the carbon emissions trading system improves energy efficiency – empirical testing based on China's provincial panel data, Energy 275 (2023) 127465.

[3] D.P. Barai, B.A. Bhanvase, S.H. Sonawane, Chapter six - compact heat exchangers, in: S.H. Sonawane, S.P. Gumfekar, B.A. Bhanvase (Eds.), Process Intensification for Chemical and Biotechnology Industries, Elsevier, 2024, pp. 101–131.

[4] O. Arsenyeva, J.J. Klemeš, L. Tovazhnyanskyy, E. Klochok, P. Kapustenko, Estimating parameters of plate heat exchanger for condensation of steam from mixture with air as a component of heat exchanger network, Energy 283 (2023) 128482.

[5] O. Arsenyeva, O. Perevertaylenko, L. Tovazhnyanskyy, P. Arsenyev, P. Kapustenko, Experimental investigation of thermal and hydraulic performance of panel plate heat exchangers, Therm. Sci. Eng. Prog. 43 (2023) 101984.

[6] D. Wang, Q. Wu, G. Wang, H. Zhang, H. Yuan, Experimental and numerical study of plate heat exchanger based on topology optimization, Int. J. Therm. Sci. 195 (2024) 108659.

[7] O. Arsenyeva, L. Tovazhnyanskyy, P. Kapustenko, J.J. Klemeš, P.S. Varbanov, Review of developments in Plate Heat exchanger heat transfer enhancement for single-phase applications in process industries, Energies (2023).

[8] L. Yicong, S. Chunyu, L. Wei, L. Zhichun, Structural parameter design of welded plate heat exchanger based on multi-objective optimization algorithm, Int. Commun. Heat Mass Tran. 146 (2023) 106900.

[9] W.W. Focke, J. Zachariades, I. Olivier, The effect of the corrugation inclination angle on the thermohydraulic performance of plate heat exchangers, Int. J. Heat Mass Tran. 28 (1985) 1469–1479.

[10] C. Zimmerer, P. Gschwind, G. Gaiser, V. Kottke, Comparison of heat and mass transfer in different heat exchanger geometries with corrugated walls, Exp. Therm. Fluid Sci. 26 (2002) 269–273.

[11] A. Muley, R.M. Manglik, Experimental study of turbulent flow heat transfer and pressure drop in a Plate Heat exchanger with chevron plates, J. Heat Tran. 121 (1999) 110–117.

[12] D. Zheng, J. Wang, Z. Chen, J. Baleta, B. Sundén, Performance analysis of a plate heat exchanger using various nanofluids, Int. J. Heat Mass Tran. 158 (2020) 119993.

[13] A. Zendehboudi, Z. Ye, A. Hafner, T. Andresen, G. Skaugen, Heat transfer and pressure drop of supercritical CO2 in brazed plate heat exchangers of the tri-partite gas cooler, Int. J. Heat Mass Tran. 178 (2021) 121641.

[14] P. Zhang, T. Ma, W.-D. Li, G.-Y. Ma, Q.-W. Wang, Design and optimization of a novel high temperature heat exchanger for waste heat cascade recovery from exhaust flue gases, Energy 160 (2018) 3–18.

[15] W. Zhang, S. Wang, L. Mu, H. Jamshidnia, X. Zhao, Investigation of the forced-convection heat-transfer in the boiler flue-gas heat recovery units employing the real-time measured database, Energy 238 (2022) 121715.

[16] X.-H. Han, L.-Q. Cui, S.-J. Chen, G.-M. Chen, Q. Wang, A numerical and experimental study of chevron, corrugated-plate heat exchangers, Int. Commun. Heat Mass Tran. 37 (2010) 1008–1014.

[17] G.I. Mahmood, P.M. Ligrani, Heat transfer in a dimpled channel: combined influences of aspect ratio, temperature ratio, Reynolds number, and flow structure, Int. J. Heat Mass Tran. 45 (2002) 2011–2020.

[18] Khail A. Aboul, A. Erişen, Heat transfer and performance enhancement investigation of novel plate heat exchanger, Therm. Sci. Eng. Prog. 34 (2022) 101368.

[19] X.-Y. Duan, M.-R. Xu, T.-P. Zhang, F.-M. Li, C.-Y. Zhu, L. Gong, Numerical analysis of the flow and heat transfer characteristics of oil-gas-water three-phase fluid in corrugated plate heat exchanger, Energy 281 (2023) 128260.

[20] N. Tran, J.-S. Liaw, C.-C. Wang, Performance of thermofluidic characteristics of recuperative wavy-plate heat exchangers, Int. J. Heat Mass Tran. 170 (2021) 121027.

[21] S. Tang, X. Xie, Z. Zhao, L. Ding, Investigation of thermal-hydraulic characteristics in a novel finned tube heat exchanger for flue gas waste heat recovery, Case Stud. Therm. Eng. 39 (2022) 102392.

[22] D.H. Nguyen, B. Kweon, J.-S. Kwon, T. Kim, S. Wongwises, H.S. Ahn, Numerical study on novel airfoil corrugated plate heat exchanger: a comparison with commercial type and geometrical parameter analysis, Int. J. Heat Mass Tran. 195 (2022) 123119.

[23] Z. Han, J. Guo, H. Zhang, J. Chen, X. Huai, X. Cui, Experimental and numerical studies on novel airfoil fins heat exchanger in flue gas heat recovery system, Appl. Therm. Eng. 192 (2021) 116939.

[24] Z. Feng, B. Su, C. Xin, T. Zhou, Y. Hao, T. Fu, Airside thermal–hydraulic performance evaluation of flue gas coolers for waste heat recovery, Appl. Therm. Eng. 228 (2023) 120433.

[25] C. Jiang, J. Wang, Y. Zhang, W. Zhou, Z. Chen, B. Bai, Condensation performance of symmetrical and parallel capsule Plate Heat exchangers, Heat Tran. Eng. 45 (2024) 1824–1835.

[26] X. Tao, Z. Zhang, T. Wu, Z. Gan, Flow boiling in dimpled plate heat exchangers with different geometric parameters: analysis of asymmetric channels, Appl. Therm. Eng. 257 (2024) 124265.

[27] U. Močnik, S. Muhič, Experimental and numerical analysis of heat transfer in a dimple pattern heat exchanger channel, Appl. Therm. Eng. 230 (2023) 120865.

[28] D.P. Soman, S. Karthika, P. Kalaichelvi, T.K. Radhakrishnan, Experimental study of turbulent forced convection heat transfer and friction factor in dimpled plate heat exchanger, Appl. Therm. Eng. 162 (2019) 114254.

[29] V.P. Carey, Liquid-Vapor Phase-Change Phenomena: an Introduction to the Thermophysics of Vaporization and Condensation Processes in Heat Transfer Equipment, Third Edition, 2020.

[30] S. Hu, X. Ma, W. Zhou, Condensation heat transfer of ethanol-water vapor in a plate heat exchanger, Appl. Therm. Eng. 113 (2017) 1047–1055.

[31] C. Bonneau, C. Josset, V. Melot, B. Auvity, Comprehensive review of pure vapour condensation outside of horizontal smooth tubes, Nucl. Eng. Des. 349 (2019) 92–108.

[32] R. Eldeeb, V. Aute, R. Radermacher, A survey of correlations for heat transfer and pressure drop for evaporation and condensation in plate heat exchangers, Int. J. Refrig. 65 (2016) 12–26.

[33] L.L. Tovazhnyanski, P. Kapustenko, Intensification of heat and mass transfer in channels of plate condensers, Chem. Eng. Commun. 31 (1984) 351–366.

[34] B. Thonon, F. Chopard, Condensation in plate heat exchangers: assessment of a general design method, in: Proceedings Eurotherm. Sem. 47th Meeting, Elsevier, Paris, 1996, pp. 10–18.

[35] W. Ambrosini, N. Forgione, A. Manfredini, F. Oriolo, On various forms of the heat and mass transfer analogy: discussion and application to condensation experiments, Nucl. Eng. Des. 236 (2006) 1013–1027.

[36] A.I. Leont'ev, Heat and mass transfer in turbulent boundary layers, in: T.F. Irvine, J.P. Hartnett (Eds.), Advances in Heat Transfer, Elsevier, 1966, pp. 33–100.

[37] S.-M. Kim, I. Mudawar, Review of databases and predictive methods for pressure drop in adiabatic, condensing and boiling mini/micro-channel flows, Int. J. Heat Mass Tran. 77 (2014) 74–97.

[38] P. Kapustenko, J.J. Klemeš, O. Arsenyeva, L. Tovazhnyanskyy, V. Zorenko, Pressure drop in two phase flow of condensing air-steam mixture inside PHE channels formed by plates with corrugations of different geometries, Energy 228 (2021) 120583.

[39] E. Nourafkan, G. Karimi, J. Moradgholi, Experimental study of laminar convective heat transfer and pressure drop of cuprous oxide/water nanofluid inside a circular tube, Exp. Heat Tran. 28 (2015) 58–68.

[40] W. Lin, W. Zhang, Z. Ling, X. Fang, Z. Zhang, Experimental study of the thermal performance of a novel plate type heat exchanger with phase change material, Appl. Therm. Eng. 178 (2020) 115630.

[41] W.-c. Lao, Y.-d. Fang, Q.-h. Chen, L.-j. Xu, H.-n. Yang, Y.-q. Huang, Experimental investigation on the flow boiling of R134a in a plate heat exchanger with mini-wavy corrugations, Int. J. Refrig. 162 (2024) 53–63.

[42] J.Y. Song, D.H. Kim, C.H. Song, Y.T. Kang, Comparisons of two-phase condensation and single-phase heat transfer and frictional pressure drop characteristics and energy-saving performance analysis of R-32 and R-410A in plate heat exchanger, Int. J. Heat Mass Tran. 231 (2024) 125813.

[43] M. Mihailović, U. Milovančević, S. Genić, B. Jaćimović, M. Otović, P. Kolendić, Air side heat transfer coefficient in plate finned tube heat exchangers, Exp. Heat Tran. 33 (2020) 388–399.

[44] H. Zhou, T. Liu, F. Cheng, D. Liu, Y. Zhu, W. Ma, Heat transfer and pressure drop performance evaluation of twisted and bent fins when steam flows through the tubes, Int. J. Heat Mass Tran. 184 (2022) 122333.

[45] W. Lee, A pressure iteration scheme for two-phase flow modeling, in: Computational Methods for Two-phase Flow and Particle Transport, WORLD SCIENTIFIC, 2013, pp. 61–82.